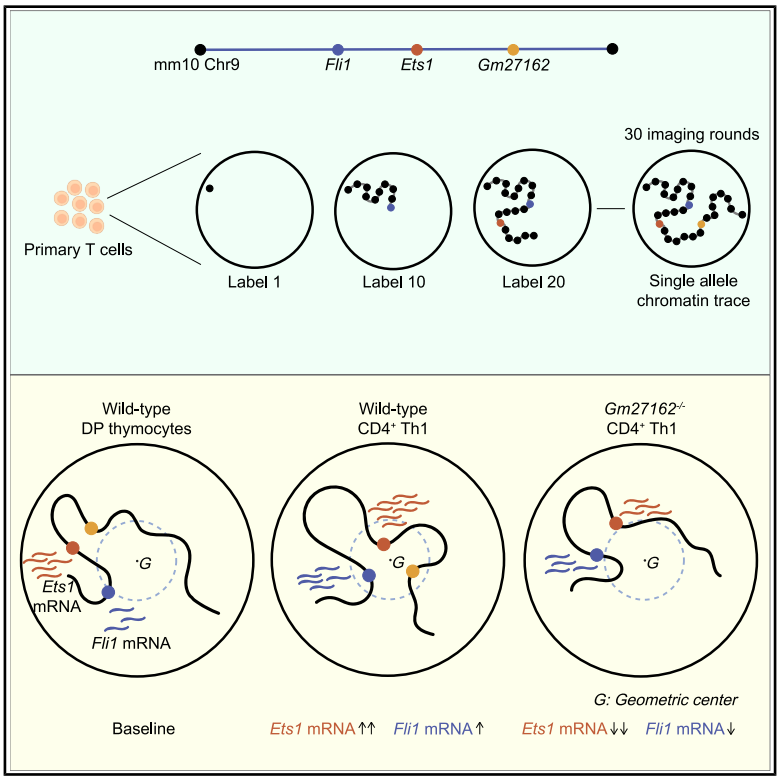
Article

Immunity

Single-allele chromatin tracing reveals cytokine-dependent super-enhancer repositioning in CD4$^+$ T cells

Graphical abstract



Highlights

- Chromatin tracing resolves multi-way *Ets1*, *Fli1*, and super-enhancer *Gm27162* contacts
- Cytokine signals reposition *Gm27162* to the geometric center of the locus
- Central *Gm27162* positioning correlates with coordinated gene expression
- Deleting the super-enhancer blocks cytokine-driven changes in locus folding

Authors

Atishay Jay, Yeqiao Zhou, Sora Yoon, ..., Arjun Raj, Robert B. Faryabi, Golnaz Vahedi

Correspondence

vahedi@pennmedicine.upenn.edu (G.V.), faryabi@pennmedicine.upenn.edu (R.B.F.)

In brief

Cytokine cues reshape how chromatin folds to control immune gene activity. Jay et al. show that cytokine signals reposition the *Ets1* super-enhancer toward the geometric center of the locus and sustain *Ets1* expression required for helper T cell differentiation, providing insight into how noncoding variants at this locus contribute to immune disorders.

Jay et al., 2026, Immunity *59*, 2483–2499
September 8, 2026 © 2026 Elsevier Inc. All rights are reserved, including those for text and data mining, AI training, and similar technologies.
https://doi.org/10.1016/j.immuni.2026.08.001

CellPress

Immunity

CellPress

Article

Single-allele chromatin tracing reveals cytokine-dependent super-enhancer repositioning in CD4$^+$ T cells

Atishay Jay,[1,2,3,6,8] Yeqiao Zhou,[3,5,7,8] Sora Yoon,[1,2,3,4,5] Bereketab N. Abeje,[1,2,3,4,5] Aditi Chandra,[1,2,3,4,5] Michael F. Michieletto,[2,7] Julia Wald,[1,3,6] Jorge Henao-Mejia,[2,7] Arjun Raj,[1,3,6] Robert B. Faryabi,[2,3,5,7,*] and Golnaz Vahedi[1,2,3,4,5,9,*]

[1]Department of Genetics, University of Pennsylvania Perelman School of Medicine, Philadelphia, PA, USA
[2]Institute for Immunology and Immune Health, University of Pennsylvania Perelman School of Medicine, Philadelphia, PA, USA
[3]Epigenetics Institute, University of Pennsylvania Perelman School of Medicine, Philadelphia, PA, USA
[4]Institute for Diabetes, Obesity and Metabolism, University of Pennsylvania Perelman School of Medicine, Philadelphia, PA, USA
[5]Abramson Family Cancer Research Institute, University of Pennsylvania Perelman School of Medicine, Philadelphia, PA, USA
[6]Department of Bioengineering, University of Pennsylvania School of Engineering and Applied Science, Philadelphia, PA, USA
[7]Department of Pathology and Laboratory Medicine, University of Pennsylvania Perelman School of Medicine, Philadelphia, PA, USA
[8]These authors contributed equally
[9]Lead contact
*Correspondence: vahedi@pennmedicine.upenn.edu (G.V.), faryabi@pennmedicine.upenn.edu (R.B.F.)
https://doi.org/10.1016/j.immuni.2026.08.001

SUMMARY

Naive CD4$^+$ T cells interpret cytokine cues to commit to T helper lineages. Here, we examined the impact of cytokines on the *Ets1-Fli1* locus, which encodes paralogous transcription factors essential for T cell effector responses. Epigenomic and chromatin interaction profiling in double-positive (DP) thymocytes defined a T cell super-enhancer and a CTCF-bound boundary. Chromatin tracing at single-allele resolution revealed concurrent multi-way interactions among *Ets1*, *Fli1*, and the super-enhancer coupled to transcription. Deleting the CTCF boundary decompacted the locus without altering *Ets1* expression or T cell development, whereas deleting the super-enhancer drew *Ets1* and *Fli1* closer; promoter proximity increased *Ets1-Fli1* co-expression. In CD4$^+$ Th1 cells, cytokines increased multi-way interactions and repositioned the super-enhancer toward the geometric center, activating both paralogs. Super-enhancer deletion rendered Th1 cells structurally and transcriptionally DP like. Thus, cytokines can drive lineage-specific gene activation by repositioning a super-enhancer, providing a mechanistic framework for how noncoding variants at the *Ets1-Fli1* locus contribute to CD4$^+$ T cell-mediated immune disorders.

INTRODUCTION

Central to adaptive immunity is the ability of CD4$^+$ T cells to differentiate and mount an effector response. This process starts by naive CD4$^+$ T cells responding to antigens and extracellular stimuli such as cytokines, differentiating into CD4$^+$ T helper subsets. The signal transducers and activators of transcription (STAT) family members are responsible for propagating integrated cytokine signals into the nucleus by operating on the chromatin landscape.[1,2] Despite extensive investigation into cytokine-mediated regulation of chromatin accessibility[3–5] and histone modifications,[6–12] the impact of cytokine signaling on the three-dimensional (3D) chromatin architecture of CD4$^+$ T helper subsets remains comparatively underexplored.[13,14] This gap largely reflects technical limitations in interrogating higher-order folding of intact chromatin at individual alleles.

Here, we traced the chromatin fiber along single alleles at the *Ets1-Fli1* locus using sequential sub-diffraction-resolution microscopy. The E26 transformation-specific (ETS) family of transcription factors represents an ancient and evolutionarily conserved group of 28 paralogous transcription factors, where some members such as *Ets1* and *Fli1* are genomically positioned in proximity as pairs. *Ets1* and *Fli1* play key roles in early hematopoiesis, T cell development, CD4$^+$ T cell differentiation, and CD8 T cell and natural killer (NK) cell responses.[15,16] A striking feature of this locus in humans is its unusual genetic association to diseases mediated by aberrant CD4$^+$ T helper cell differentiation including allergy, asthma, lupus, and rheumatoid arthritis.[17] A cluster of immune disease-associated polymorphisms at this locus co-localizes with a T cell-specific super-enhancer and overlaps a long noncoding RNA (annotated as *ENSG00000307544* in humans and *Gm27162* in mice). However, why genetic variation in noncoding elements at this locus predisposes individuals to CD4$^+$

All rights are reserved, including those for text and data mining, AI training, and similar technologies.

T cell-mediated immune diseases is not well understood. Previously, we showed that genetic deletion of the T cell-specific super-enhancer *Gm27162* in mice does not affect T cell development but limits $CD4^+$ T helper 1 (Th1) differentiation and makes mice susceptible to allergic inflammation.[18] But how cytokine signaling and genetic perturbation remodel the chromatin fiber of this locus remained unresolved. Answering this question can provide a mechanistic link between genetic variation, 3D chromatin architecture, and dysregulated $CD4^+$ T cell function underlying immune-mediated diseases.

In this study, we utilized a sequential sub-diffraction-resolution imaging approach termed optical reconstruction of chromatin architecture (ORCA),[19–23] tracing the *Ets1-Fli1* locus at single-allele resolution. We also combined ORCA with single-molecule RNA fluorescence *in situ* hybridization (smRNA-FISH) to simultaneously trace folding of individual *Ets1-Fli1* chromatin fibers and relate the locus topology to expression of both *Ets1* and *Fli1* genes. We first traced the chromatin of thymocytes to establish a baseline of chromatin folding in thymic DP T cells and its relationship to *Ets1* and *Fli1* mRNA levels. Building on this reference, we showed that Th1-polarizing cytokines drove radial repositioning of the *Gm27162* super-enhancer toward the geometric center of the locus. This repositioning coincided with increased formation of multi-way interactions between the *Ets1* and *Fli1* promoters and the super-enhancer, accompanied by increased expression of both paralogs. Strikingly, *Gm27162*-deleted Th1 cells failed to adopt the wild-type Th1 chromatin configuration and instead retained an architecture resembling that of *Gm27162*-deleted thymocytes. Thus, cytokine-mediated signaling can license super-enhancers through changes in local chromatin positioning to drive increased transcription. These findings provide a structural framework for understanding how disease-associated genetic variants at the *Ets1-Fli1* locus may perturb super-enhancer positioning and multi-way enhancer-promoter interactions in *cis*, thereby altering paralog expression and predisposing to $CD4^+$ T cell-mediated immune disorders.

RESULTS

Epigenomic profiling of the *Ets1-Fli1* locus

Previously,[24] we used H3K27ac HiChIP to map enhancer-enhancer interactions and found that the genomic region harboring the *Ets1* and *Fli1* genes is exceptionally connected in thymocytes, classified as a hyperconnected 3D clique[24,25] or multi-enhancer hub.[18] Consistent with this connectivity, H3K27ac accumulated across the *Ets1* and *Fli1* promoters and gene bodies, as well as over a 25-kbp segment downstream of *Ets1*, annotated as the lncRNA *Gm27162*, which scored as a super-enhancer in thymocytes, naive $CD4^+$ T cells, and differentiated T helper cells. To define the chromatin context of this hub, we profiled the repressive modification H3K27me3 by performing cleavage under targets & release using nuclease (CUT&RUN[26]) in double-positive (DP) $CD4^+CD8^+$ T cells from the mouse thymus (Figure 1A). The enhancer connectivity spanning *Ets1* and *Fli1* was confined to a continuous stretch of H3K27ac flanked by two H3K27me3 domains ~750 kbp apart (Figure 1A). We also identified CTCF occupancy at 100 kbp upstream of the *Ets1* promoter, in addition to 245 and 390 kbp downstream of this gene, placing boundary elements at two ends of the active hub.

To measure folding dynamics of the chromatin fiber at single-allele resolution, we utilized two genetic models. We used our previously generated mouse strain lacking the T cell-specific super-enhancer ($Gm27162^{-/-}$ also $Ets1\text{-}SE^{-/-}$ in Chandra et al.[18], pink bar, Figure 1A). We also generated a new strain, CTCF binding site (CBS) +245kbp$^{-/-}$, in which we deleted a 6.2 kbp region enriched for CTCF binding sites located 245 kbp downstream of the *Ets1* promoter (blue bar, Figure 1A). Together, the $Gm27162^{-/-}$ and CBS +245kbp$^{-/-}$ models provided complementary tools to dissect how a super-enhancer and a boundary element shape chromatin architecture and gene regulation at this locus.

We performed population-based sequencing assay HiC[27,28] across genotypes in DP T cells (Figures 1B–1F). Examination of HiC contact-frequency map in wild-type DP T cells showed the establishment of three domains insulated by CBSs and significant interactions between *Ets1* and its super-enhancer, *Gm27162* (Figure 1B). The largest domain structure that encompassed *Ets1* and *Gm27162* was bordered by convergent CTCF binding motifs 100 kbp upstream and 245 kbp downstream of the *Ets1* promoter (Figure 1A, arrows represent CTCF motif orientation). $Gm27162^{-/-}$ DP T cells showed fewer long-range interactions compared with wild-type cells (Figures 1C and 1E). The deletion of CBS +245kbp at the boundary of H3K27ac and H3K27me3 domains led to loss of insulation between the two repressed domains (Figures 1D and 1F). Together, the population-level HiC data suggested broad changes in chromatin organization at the *Ets1-Fli1* locus after genetic perturbation.

Ensemble of ORCA traces reproduces chromatin architecture detected in HiC

HiC captures pairwise contacts averaged across millions of cells and cannot directly resolve concurrent multi-way interactions within the same allele. To trace the intact chromatin fiber at the single-allele level using ORCA,[19–23] we designed primary probes to tile a 900 kbp window at a 30 kbp resolution. Successful hybridization was confirmed by illumination of the "fiducial" signal, labeling all "primary probes" in the domain, and 30 unique "readout probes" for each 30 kbp segment (Figure 2A). Each trace was resolved into 30 coordinates in 3D, producing positions of a contiguous series of chromatin segments—termed a chromatin "walk"—that together delineates the spatial conformation of the *Ets1-Fli1* locus. We optimized the hybridization efficiency of probes and hence the full-trace detection percentage, which allowed us to exclude chromatin traces that missed hybridization to any readout probes (Figures S1A and S1B). To assess the quality of our imaging-based approach, we pooled chromatin traces measured by ORCA and mapped average pairwise distances. This analysis generated a similar pattern of domains, loops, and stripes as observed in the contact-frequency map from HiC ($r = 0.86$, Figure 2B). To compare ORCA with HiC, we defined "interactions" in our chromatin tracing measurements based on 3D distances falling below a stringent threshold (<150 nm).[21,23] The contact-frequency matrix generated by ORCA based on thresholding 3D distances correlated highly with the contact-frequency matrix generated by HiC ($r = 0.9$, Figure 2C). We also reported strong reproducibility for

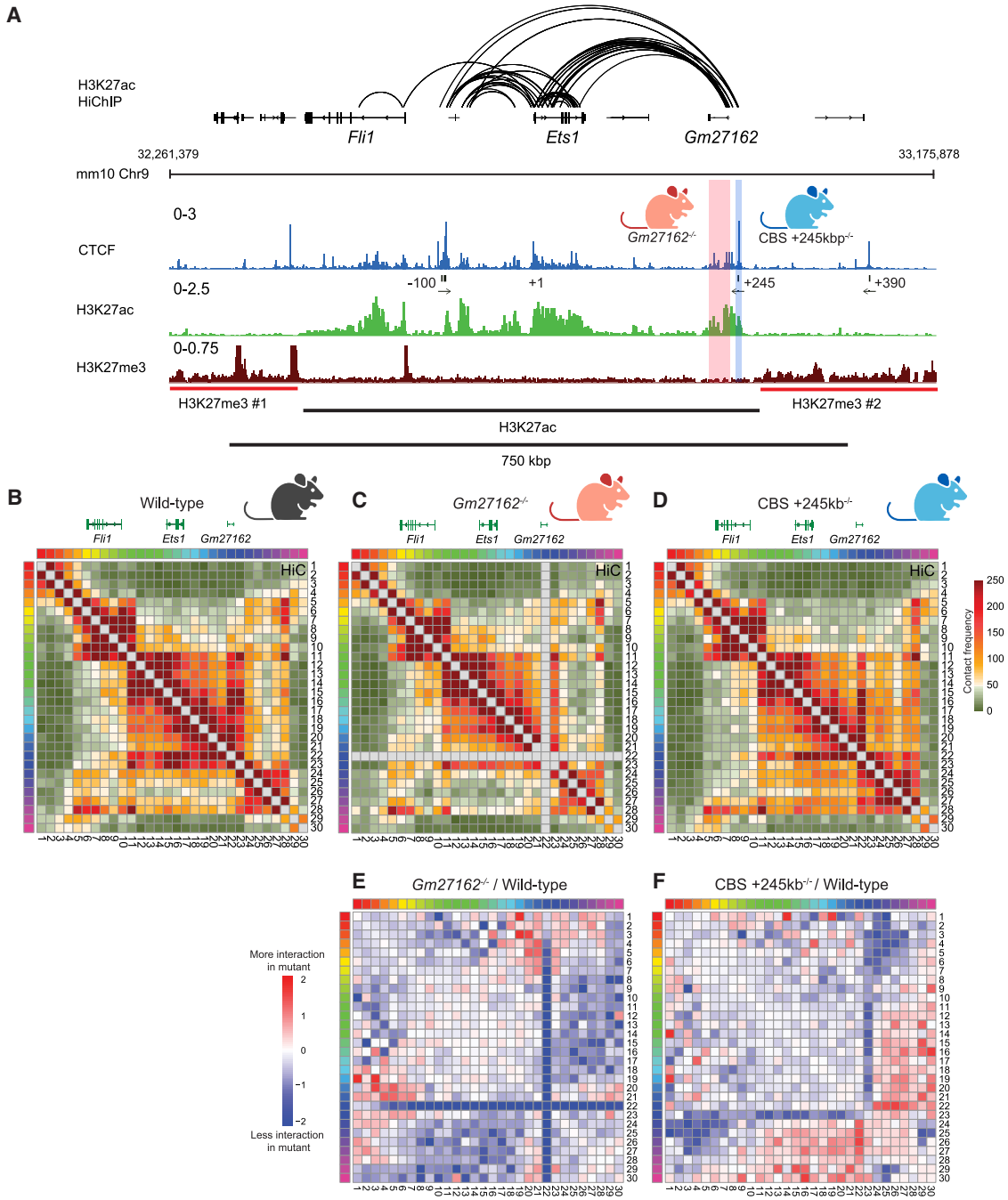


Figure 1. Enhancer connectivity at the *Ets1-Fli1* locus is flanked by H3K27me3-rich repressed chromatin

(A) Histone modifications and CTCF binding in CD4^{+}CD8^{+} double-positive (DP) T cells measured by CUT&RUN; arrows annotate prominent CTCF peaks relative to the *Ets1* promoter; curved lines show enhancer-enhancer interactions by H3K27ac HiChIP. Pink bar, 25-kbp deletion in *Gm27162*$^{-/-}$ mice; blue bar, 6.2-kbp CTCF binding site (CBS) deletion in CBS +245kbp$^{-/-}$ mice.

(B–D) HiC contact heatmaps of (B) wild-type, (C) *Gm27162*$^{-/-}$, and (D) CBS +245kbp$^{-/-}$ DP T cells at 30-kbp resolution.

(E and F) HiC difference heatmaps comparing (E) *Gm27162*$^{-/-}$ or (F) CBS +245kbp$^{-/-}$ with wild-type DP T cells; color bar, interaction state in the mutant relative to wild type.

our chromatin tracing experiments in two biological replicates (Figures S1C and S1D). Throughout this study, we performed experiments in two biological replicates and pooled thousands of individual chromatin traces across replicates. Together, our ORCA-based chromatin tracing experiments closely recapitulated the chromatin architecture observed in population-level HiC assays, while adding single-allele insights into intact chromatin organization.

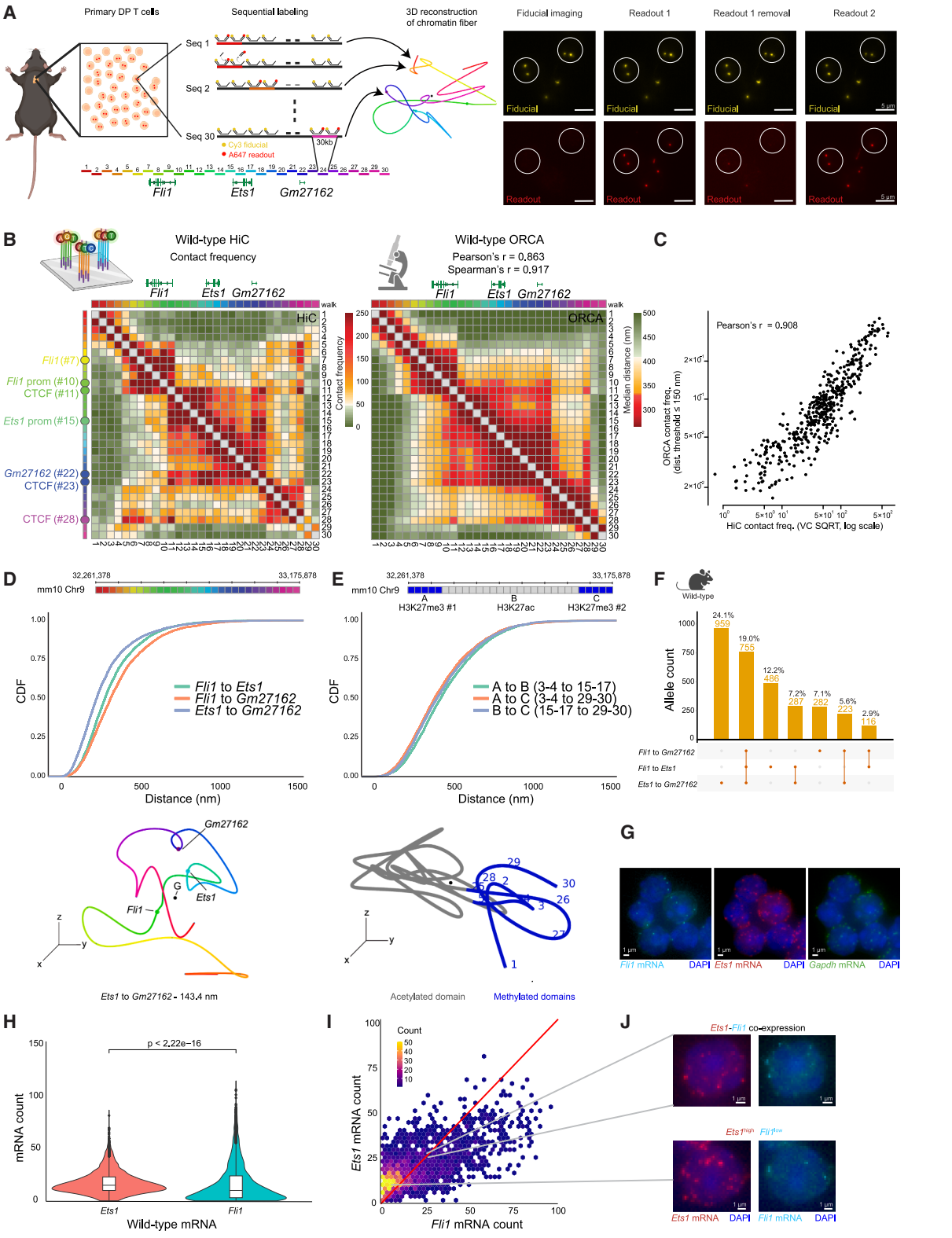


Figure 2. ORCA reveals multi-way enhancer-promoter interactions in DP T cells

(A) Schematic of ORCA: pseudo-colored 30-kbp readouts tiling the *Ets1-Fli1* locus in thymic DP T cells, with representative reference (fiducial) and readout images; scale bar, 5 μm.

(legend continued on next page)

ORCA reveals multi-way enhancer-promoter interactions in DP T cells

We next used this single-allele resolution approach to quantify regulatory domain interactions by directly measuring 3D distances between domains in individual DP T cells. For genomic regions of interest extending beyond 30 kbp and spanning multiple readout probes, we determined the geometric centers, also called "centroids," and calculated the Euclidean distances between centroids per allele. Cumulative distance distribution analysis across single alleles for the centroids of *Ets1*, *Fli1*, and *Gm27162* showed that the *Ets1* gene is most frequently positioned near its super-enhancer *Gm27162* in DP T cells (mean distance = 285.3 nm, Figure 2D top), as seen in a representative chromatin trace (Figure 2D bottom). Surprisingly, the 3D distance between the two flanking H3K27me3-marked regions (mean = 438.4 nm) was smaller compared with the 3D distance between regions with opposite histone modifications despite a linear genomic distance of 750 kbp between the two H3K27me3 regions (mean = 450.7 or 472.4 nm, Figure 2E, top). A representative trace showcased this trend (Figure 2E, bottom). This spatial proximity for H3K27me3 regions was not detected in bulk HiC experiments (Figure 1), suggesting that our microscopy technique can overcome HiC's limited enzymatic capture radius.

Since the *Ets1-Fli1* locus scored as a multi-enhancer hub in our bulk HiChIP analysis,[24] we next quantified multi-way connectivity within this locus for individual alleles. Interactions were defined based on 3D distances for individual alleles falling below a threshold. For each experiment, we defined the threshold as the average distance between consecutive readouts as the interaction cutoff.[21] We detected *Ets1-Gm27162* interactions in 24% of alleles and *Ets1-Fli1* interactions in 12% of alleles (Figure 2F). Three-way interactions between *Ets1*, *Fli1*, and *Gm27162* regions occurred in ~19% of alleles (Figure 2F). According to HiC and HiChIP,[24] CTCF binding sites frequently interacted with H3K27ac-rich regions including the *Ets1* promoter. Using ORCA, we observed that CTCF binding sites colocalized with H3K27ac-rich regions in ~12% of our alleles (Figure S1E). These 5-way interactions occurred at a frequency ~5.5 times higher than those previously reported for the *Sox2* locus in mouse embryonic stem cells[21] (Figure S1E). Thus, although the most frequent topology in DP T cells related to spatial localization of *Ets1* and *Gm27162* and their separation from *Fli1*, multi-way interactions of *Ets1*, *Gm27162* and *Fli1* were also detected in a percentage of alleles.

smRNA FISH indicates high *Ets*1 and low *Fli1* mRNA levels in DP T cells

Next, we performed single-molecule (sm)RNA FISH to quantify the expression of *Ets1* and *Fli1* in DP T cells (Figures 2G–2J). Robustness of our smRNA FISH for *Ets1* and *Fli1* was evident from consistent detection of *Gapdh* across multiple fields of view with simultaneous measurement of *Ets1* and *Fli1* in the same cells (Figure S1F). *Ets1* mRNA molecules were 50% more abundant than *Fli1* mRNA molecules (median *Ets1* = 15 and *Fli1* = 10) (Figure 2H). Quantification of *Ets1* and *Fli1* transcripts within individual cells revealed an enrichment of cells characterized by high *Ets1* and low *Fli1* expression, which we defined as *Ets1*^{high}*Fli1*^{low} cells. There was also a small subset of cells with comparable levels of *Ets1* and *Fli1* expression (Figure 2I). In comparison to *Ets1*^{high}*Fli1*^{low} cells, the *Fli1-Ets1*-co-expressing cells exhibited more *Fli1* mRNA spots (Figure 2J). Overall, transcriptional outputs of *Ets1* were higher than those of *Fli1* in DP T cells.

Loss of CTCF boundary drives domain-wide decompaction in DP T cells

We next examined how deleting a CTCF-occupied boundary element affected the locus. Loss of CBS +245 kbp led to the spread of H3K27ac into the previously H3K27me3-rich domain (dashed box, Figure 3A). The spread of H3K27ac was contained by another CTCF binding site at ~390 kbp downstream of the *Ets1* promoter, which demonstrated an increase in CTCF occupancy and formed a strong boundary in CBS +245kbp$^{-/-}$ T cells (red bar, Figure 3A). Together, the chromatin state of the locus shifted from a repressed state in wild-type cells to an active state in CBS +245kbp$^{-/-}$ cells.

To examine the role of this putative insulator element in organizing folding of the *Ets1-Fli1* locus, we then performed ORCA experiments in CBS +245kbp$^{-/-}$ DP T cells. The ensemble of ORCA traces reproduced the genome organization observed in HiC contact maps with high reproducibility (Figures 3B, 3C, and S2A–S2C). Thus, we examined the contribution of CBS +245 kbp to the relative spatial position of *Ets1*, *Fli1*, and *Gm27162*. While *Ets1* and *Gm27162* remained the most proximal interacting enhancer-promoter pair, the loss of CBS +245 kbp increased the mean distance between any pair of *Ets1*, *Fli1*, and *Gm27162* by at least 50 nm (Figure 3D). Moreover, the distance between H3K27me3 domains increased after CBS +245 kbp deletion (438.4 nm in wild-type and 493.9 nm in CBS + 245kbp$^{-/-}$, Figure 3E). Representative ORCA chromatin traces showed

(B) Wild-type HiC contact-frequency map (30-kbp bins, left) and ORCA median-distance matrix (right); color bars, contact-frequency and median distance; Pearson's and Spearman's r, correlation.
(C) HiC-ORCA contact-frequency correlation (Pearson's r; ORCA threshold, 150 nm). ORCA was performed in two biological replicates and traces were pooled for analysis.
(D) Top, cumulative centroid-distance distributions (nm) for *Fli1-Ets1* (green, mean 332.0), *Fli1-Gm27162* (orange, 372.0), and *Ets1-Gm27162* (blue, 285.3). Bottom, representative ORCA trace (*Ets1-Gm27162*, 143.4 nm).
(E) Top, cumulative distance distributions between domains defined in Figure 1A: methylated #1 (A)—acetylated (B) (green, mean 472.4 nm), A—methylated #2 (C) (orange, 438.4 nm), B and C (blue, 450.7 nm). Bottom, representative ORCA trace.
(F) Upset plot of the frequency and allele number of three-way *Ets1-Fli1-Gm27162* interactions (contact threshold, 257.89 nm; 3,979 traces).
(G) Representative single-molecule RNA FISH of *Fli1* (cyan), *Ets1* (red), and *Gapdh* (green) mRNA with 4',6-diamidino-2-phenylindole (DAPI) (blue) in DP T cells. Scale bar, 1 μm.
(H) Violin plot of *Ets1* and *Fli1* mRNA counts in wild-type DP T cells (two-sided Wilcoxon rank-sum test).
(I) 2D histogram of smRNA-FISH *Ets1* versus *Fli1* mRNA per wild-type DP T cell; color bar, cell number per bin.
(J) Representative smRNA-FISH images of *Ets1-Fli1* co-expressing (top) and *Ets1*-high *Fli1*-low (bottom) cells mapped to their positions in (I). Scale bar, 1 μm.

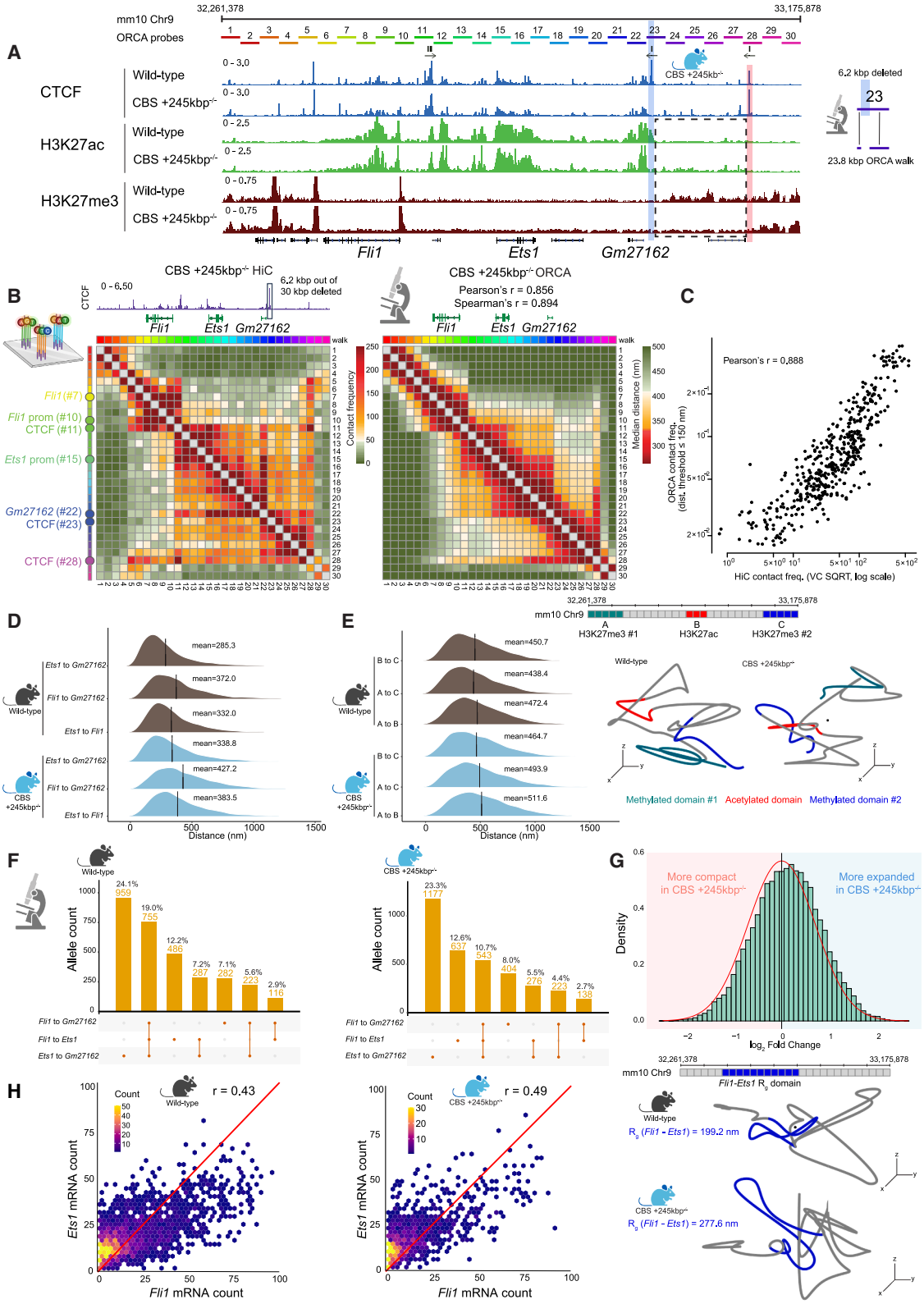


Figure 3. Loss of CTCF boundary drives domain-wide decompaction in DP T cells

(A) Genome-browser views of histone modifications and CTCF occupancy within the *Ets1-Fli1* hub in wild-type and CBS +245kbp$^{-/-}$ DP T cells (CUT&RUN); blue bar, 6.2 kbp CBS deletion at the H3K27ac-H3K27me3 interface (+245 kbp from the *Ets1* promoter); pink bar, increased occupancy of CTCF at a site +390 kbp

(legend continued on next page)

intermixing between H3K27ac and the *de novo* H3K27ac chromatin domains (Figure 3E). Loss of CBS +245 kbp also reduced three-way interactions among *Ets1*, *Fli1*, and *Gm27162* (~19% to 10%, Figure 3F) and multi-way interactions involving promoters, enhancers, and CTCF-bound elements (12.4% to 5.4%, Figure S2D). We also computed the radius of gyration (R_g), a measure of the spatial distribution of chromatin relative to its center of mass,[29,30] for each chromatin trace (Figure S2E). This analysis showed a higher frequency of expanded chromatin traces in CBS +245kbp$^{-/-}$ compared to wild-type DP T cells for both its immediate 5′ region (Figure S2F) and ~400 kbp upstream region encompassing *Fli1* and *Ets1* (Figure 3G, top), as visualized by representative chromatin traces (Figure 3G, bottom). Collectively, loss of CBS +245 kbp led to chromatin decompaction.

CTCF boundary deletion leaves T cell development and *Ets1* expression intact

We next asked whether this chromatin decompaction had any functional consequences for thymocytes by measuring the extent to which *Ets1* and *Fli1* mRNA production was affected by deletion of CBS +245 kbp. Our smRNA FISH measurements did not detect any significant change in *Ets1* production relative to wild-type DP T cells (median CBS +245kbp$^{-/-}$ = 14 and wild-type = 15, Figure 3H, right), in line with the observation of marginal reduction in the frequency of chromatin fibers with *Ets1-Gm27162* interactions (23.3% in CBS +245kbp$^{-/-}$ and 24.1% in wild-type DP T cell, Figure 3F). Nevertheless, there was a reduction in the proportion of *Fli1*^{high} cells, marked by a decrease in average *Fli1* mRNA expression (median in CBS + 245kbp$^{-/-}$ = 6 and wild-type = 10, Figures S2G and S2H). Consistent with a marginal reduction in *Ets1* expression, no major alterations were observed in the developmental trajectories of T cells in the thymus of CBS +245kbp$^{-/-}$ mice (Figure S2I). Thus, domain-wide decompaction of the *Ets1-Fli1* enhancer hub in CBS +245kbp$^{-/-}$ T cells had minimal impact on *Ets1* expression or T cell development.

Gm27162 deletion leads to spatial proximity of *Ets1* and *Fli1* gene loci in DP T cells

To distinguish the contribution of enhancers from boundary architecture, we next examined the chromatin state following deletion of the *Gm27162* super-enhancer. Histone modifications H3K27ac and H3K27me3 did not change after super-enhancer deletion (Figure 4A). To trace the *Ets1-Fli1* locus in *Gm27162*$^{-/-}$ DP T cells, we hybridized the same set of primary probes used in wild-type cells and only selected chromatin traces with 30 successful hybridizations (Figure S3A). We employed the 30 kbp hybridization scheme at the locus harboring *Gm27162* to specifically capture a 5 kbp region flanking the deleted region (referred to as deletion flanking region [DFR]) (Figure S3B). The contact-frequency matrix based on pooled alleles measured by ORCA in *Gm27162*$^{-/-}$ mice correlated strongly with HiC, and the imaging results were highly reproducible (Figures 4B, 4C, S3C, and S3D).

To examine the impact of *Gm27162* super-enhancer deletion on distal chromatin interactions, we computed the distribution of centroid distances between *Ets1*, *Fli1* gene loci, and *Gm27162*. Interestingly, the *Gm27162* super-enhancer deletion positioned the *Ets1* and *Fli1* gene bodies closer to each other (mean wild-type = 332 nm and *Gm27162*$^{-/-}$ = 314.2 nm, Figure 4D). This increased proximity was also observed when focusing specifically on the readouts corresponding to the *Ets1* and *Fli1* promoters (Figure S3E). Additionally, the *Ets1* gene locus was further away in 3D distance from the *Gm27162* DFR (mean wild-type = 285.3 nm and *Gm27162*$^{-/-}$ = 368 nm, Figure 4D). Representative ORCA chromatin traces corroborated this observation (Figure 4D, right). Distance between H3K27me3 modified regions did not change significantly in *Gm27162*$^{-/-}$ compared with wild-type cells (Figure 4E). We computed the radius of gyration and found an increased frequency of chromatin traces where the region spanning *Ets1* and *Fli1* was more compact in *Gm27162*$^{-/-}$ DP T cells compared to wild-type counterparts (Figure S3F). To further quantify this reorganization, we assessed the frequency of multi-way interactions between *Fli1*, *Ets1*, and the *Gm27162* DFR (Figure 4F). Loss of *Gm27162* reduced both three-way interactions (19% to 14%) and *Ets1-Gm27162* DFR contacts (24% to 14%) (Figure 4F). In contrast, spatial proximity of *Fli1* and *Ets1* increased in *Gm27162*$^{-/-}$ DP T cells (12% to 20%) (Figure 4F). Thus, *Gm27162* deletion shifted interaction frequencies from super-enhancer-*Ets1* contacts toward *Ets1-Fli1* association.

Loss of *Gm27162* leads to increased co-expression of *Ets1* and *Fli1* mRNA

Observing the impact of *Gm27162* deletion on positioning of *Ets1* and *Fli1* led us to evaluate the functional consequences of this super-enhancer deletion on gene expression using smRNA-FISH. *Gm27162* deletion increased the number of cells with *Ets1* and *Fli1* co-expression at the expense of *Ets1*^{high}*Fli1*^{low}

downstream of *Ets1* promoter; the schematic (right) shows the deletion within readout 23 (remaining 23.8 kbp imaged by ORCA). Dashed box, *de novo* H3K27ac spreading into the H3K27me3 domain.

(B) HiC contact-frequency/ORCA median distance maps for CBS +245kbp$^{-/-}$ DP T cells; CTCF track marks the deleted ORCA-bin fraction. ORCA was performed in two biological replicates and traces were pooled for analysis.

(C) HiC-ORCA contact-frequency correlation for CBS +245kbp$^{-/-}$ DP T cells.

(D) Density plots for centroid distances for *Fli1-Ets1*, *Fli1-Gm27162*, and *Ets1-Gm27162* in wild-type (brown, top) and CBS +245 kbp$^{-/-}$ (blue, bottom) DP T cells.

(E) Left, density plots between domains (A–B, A–C, and B–C) in wild-type (brown, top) and CBS +245kbp$^{-/-}$ (blue, bottom) DP T cells. Middle and right, representative ORCA traces per genotype; color bar, methylated #1 (green), acetylated (red), and methylated #2 (blue) positions.

(F) Upset plots of multi-way interaction frequency in wild-type (threshold 257.89 nm; 3,979 traces) and CBS +245kbp$^{-/-}$ (threshold 262.13 nm; 5,059 traces) DP T cells.

(G) Top, histogram of $\log_2$ fold change in local radius of gyration (R_g) between CBS +245 kbp$^{-/-}$ and wild-type DP T cells (bootstrapping 1,000 alleles per genotype over 1,000 iterations); red area, more compact; blue area, more expanded; red curve, normal distribution. Middle and bottom, representative wild-type and CBS +245kbp$^{-/-}$ ORCA traces.

(H) 2D histograms of smRNA-FISH counts for wild-type (left) and CBS +245kbp$^{-/-}$ (right) DP T cells. Pearson's r, *Ets1-Fli1* expression correlation.

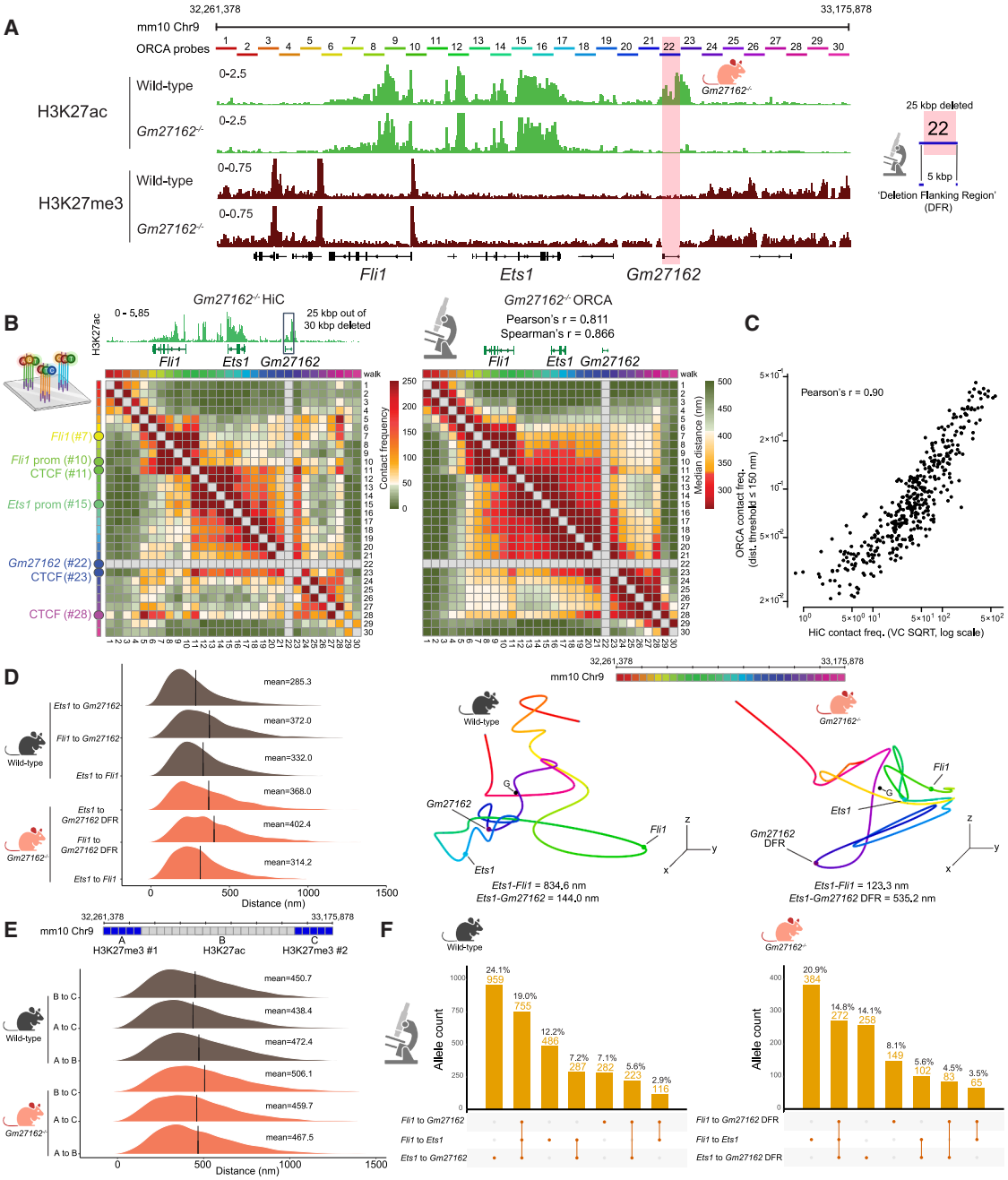


Figure 4. Deletion of the *Ets1* super-enhancer *Gm27162* leads to spatial proximity of *Ets1* and *Fli1* promoters

(A) Genome-browser view of H3K27ac and H3K27me3 (CUT&RUN) within the *Ets1-Fli1* hub in *Gm27162*$^{-/-}$ DP T cells; 30-kbp ORCA readouts overlaid on a genome scale. Pink bar, 25-kbp *Gm27162* deletion; the schematic (right) shows the deletion within readout 22, with the remaining 5 kbp defined as the *Gm27162* deletion flanking region (DFR).

(B) HiC contact-frequency/ORCA median distance maps for *Gm27162*$^{-/-}$ DP T cells; H3K27ac track marks the deleted region. ORCA was performed in two biological replicates, and traces were pooled for analysis.

(C) HiC-ORCA contact-frequency correlation for *Gm27162*$^{-/-}$ DP T cells.

(D) Density plots for ORCA centroid-distance distributions for *Fli1-Ets1*, *Fli1-Gm27162*, and *Ets1-Gm27162* in wild-type (brown, top) and *Gm27162*$^{-/-}$ (orange, bottom) DP T cells; representative *Gm27162*$^{-/-}$ (right) and wild-type (middle) ORCA traces.

(E) Density plots of ORCA distance distributions between domains (A–B, A–C, and B–C) in wild-type (brown, top) and *Gm27162*$^{-/-}$ (orange, bottom) DP T cells.

(F) Upset plots of multi-way interaction frequency in wild-type (threshold 257.89 nm; 3,979 traces) and *Gm27162*$^{-/-}$ (threshold 260.99 nm; 1,834 traces) DP T cells.

DP T cells (r = 0.43 in wild-type versus r = 0.58 in *Gm27162*$^{-/-}$, Figures 5A–5C). To further quantitate the co-expression of these two paralogs, we stratified cells into *Fli1*^{high} (>15 transcripts) and *Fli1*^{low} cells (<15 transcripts) and compared *Ets1* expression distributions for each group (Figure S4A). In *Fli1*^{high} cells, *Ets1* was highly expressed in both genotypes. However, there was a 25% reduction in *Ets1* level in *Gm27162*$^{-/-}$ *Fli1*^{high} cells (median wild type = 23, *Gm27162*$^{-/-}$ = 17). In *Fli1*^{low} cells, we detected a ~75% reduction in *Ets1* expression in *Gm27162*$^{-/-}$ cells relative to wild-type cells (median wild type = 12, Gm27162$^{-/-}$ = 3) (Figure S4A). Visual inspection of representative *Ets1*^{high}*Fli1*^{high} cells in *Gm27162*$^{-/-}$ DP T cells confirmed this observation (Figures S4B and S4C). Thus, loss of *Gm27162* reinforced *Ets1-Fli1* transcriptional coupling, functionally linking *Fli1* expression to *Ets1* levels.

Combined RNA-DNA FISH in DP T cells links co-expression of *Ets1* and *Fli1* mRNA to spatial proximity of promoters

So far, our RNA and DNA FISH measurements were performed in separate cells, preventing a direct mechanistic link between chromatin proximity and transcriptional output. To address this limitation, we modified the ORCA workflow to quantify mRNA abundance prior to chromatin tracing within the same cells. We isolated DP T cells, fixed them on a coverslip and first labeled *Ets1* and *Fli1* mRNA molecules. Following imaging of hybridized mRNA, we denatured DNA and hybridized ORCA probes spanning the *Ets1-Fli1* locus. This time, we only used readout probes corresponding to the *Ets1* promoter, *Fli1* promoter, and *Gm27162*. Utilizing this approach, we quantified the cell position, its associated mRNA counts for both genes and the 3D distances between *Ets1* promoter, *Fli1* promoter, and *Gm27162* for each cell (Figure 5D). Representative images showed successful alignment of *Ets1* and *Fli1* mRNA with the fiducial and readout signals from ORCA measurements, generating RNA-DNA imaging composite per cell (Figure 5E). We compared *Ets1* and *Fli1* mRNA distributions between RNA-only FISH and combined RNA-DNA FISH and observed strong agreement between the two methods. In wild-type DP T cells, median *Ets1* expression was similar (15 versus 17), as was *Fli1* expression (10 versus 10), with comparable concordance in *Gm27162*$^{-/-}$ cells (Figures 5C and 5F).

In order to classify the critical chromatin interactions driving mRNA production, we leveraged the ORCA measurements to cluster cells based on the interaction state between the *Fli1* promoter, *Ets1* promoter, and *Gm27162* and evaluated the *Ets1* and *Fli1* mRNA counts in each cluster. In the case of *Ets1* expression, alleles were classified into four groups: no interaction among *Ets1*, *Fli1*, and *Gm27162*; *Ets1-Gm27162* interaction only; *Ets1-Fli1* interaction only; and concurrent interactions of *Ets1* with both *Fli1* and *Gm27162*. Multi-way contact between the *Ets1* promoter, *Fli1* promoter, and *Gm27162* increased *Ets1* production over other combinations (median = 18, Figure 5G). High levels of *Ets1* mRNA expression also coincided with the *Ets1* promoter interacting with its super-enhancer *Gm27162* (median = 17.0, Figure 5G). DP T cells lacking *Gm27162* showed reduced expression of *Ets1* mRNA across all clusters (median *Gm27162*$^{-/-}$ = 11, wild type = 17, Figures 5F and 5G).

Differences in mean *Ets1* mRNA molecules across interaction groups were modest. This was not unexpected, as our RNA FISH assay quantified total cellular mRNA rather than allele-specific transcripts. Consequently, variability in chromatin architecture at individual alleles can complicate DNA-RNA linkage analysis. We therefore reasoned that restricting the analysis to cells with the highest mRNA levels might better resolve allele-specific chromatin behavior. Thus, we quantified the proportion of *Ets1*^{high} cells within each interaction category (i.e., *Ets1* expression > 25 molecules). In *Ets1*^{high} DP T cells, 65% of alleles exhibited *Ets1* promoter interaction with *Gm27162*, either exclusively or as part of a multi-way hub with *Fli1* (Figure 5H). *Ets1*^{high} cells driven by *Ets1-Fli1* promoter-promoter contacts were restricted to 16% of wild-type DP T cells (Figure 5H). In *Gm27162*$^{-/-}$ DP T cells, the proportion of *Ets1*^{high} cells driven by *Ets1-Fli1* promoter interactions increased by 30%, accompanied by a 27% reduction associated with *Gm27162-Ets1* interactions. Extending beyond thresholding of *Ets1* expression, stratification of cells by graded *Ets1* mRNA abundance further corroborated the association between high transcriptional output and preferential *Ets1-Gm27162* proximity (Figure S4D).[31]

We also evaluated how chromatin interactions drove *Fli1* mRNA production (Figure S4E). We first isolated *Fli1*^{high} cells (*Fli1* mRNA > 15 molecules) and plotted the distribution of distance between *Ets1* and *Fli1* promoters in wild-type and *Gm27162*$^{-/-}$ DP T cells (Figure 5I). *Fli1*^{high} cells had a lower mean distance between the two promoters in *Gm27162*$^{-/-}$ DP T cells compared with wild-type cells (357 versus 426 nm, Figure 5I). In *Fli1*^{high} cells, the *Ets1* and *Fli1* co-expression in the same cell increased in *Gm27162*$^{-/-}$ DP T cells relative to wild-type DP T cells (r = 0.61 versus r = 0.42, Figure 5I). Thus, *Ets1-Fli1* promoter-promoter proximity correlated with an increase in the co-expression of both genes in the absence of *Gm27162* in DP T cells.

Chromatin tracing in CD4$^+$ Th1 cells

Our primary goal in this study was to determine how cytokine signaling remodels the chromatin fiber of the *Ets1-Fli1* locus. So far, we established a baseline for the chromatin fiber configuration and transcriptional regulation at this locus in DP T cells. Building on this foundation, we next investigated whether the regulatory logic governing this locus in thymocytes was maintained during Th1 differentiation or instead fundamentally reconfigured as cells adopt the Th1 fate. Because deletion of the *Gm27162* super-enhancer impairs CD4$^+$ Th1 cell differentiation,[18] we focused our analysis on this perturbation, in comparison with the deletion of the CBS +245 kbp element, which did not affect Th1 differentiation (Figures S5A and S5B) and was therefore not pursued further. We performed ORCA-based chromatin tracing on *in vitro* polarized CD4$^+$ Th1 cells from wild-type and *Gm27162*$^{-/-}$ mice. Naive CD4$^+$ T cells from each strain were polarized *in vitro* in the presence of CD3/CD28 antibodies activating T cell receptor (TCR) in addition to cytokines IL-2, IL-12, and anti-IL-4. Polarized CD4$^+$ Th1 cells were harvested and fixed 6 days after stimulation for subsequent imaging experiments (Figure 6A). The same set of primary probes used in DP T cells was applied for chromatin tracing in CD4$^+$ Th1 cells, yielding robust hybridization with high detection efficiency as evidenced by strong fiducial and readout signals (Figures 6B and S5C). The average pairwise distance matrix of pooled chromatin traces from wild-type and *Gm27162*$^{-/-}$ CD4$^+$ Th1 cells correlated

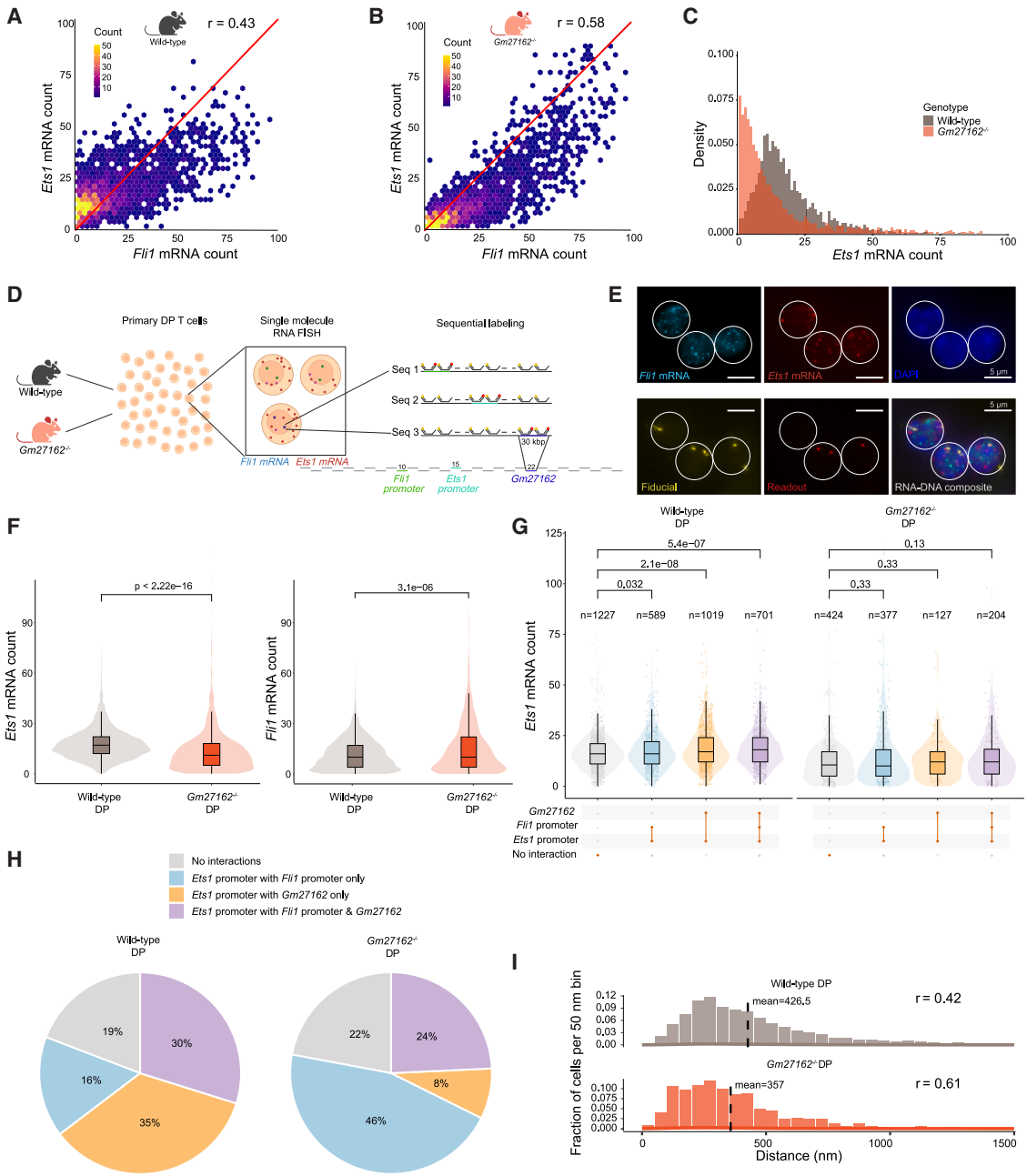


Figure 5. Combined RNA-DNA FISH in DP T cells links co-expression of *Ets1* and *Fli1* mRNA to promoter spatial proximity

(A and B) 2D histograms show *Ets1* and *Fli1* smRNA-FISH counts for (A) wild-type and (B) *Gm27162*$^{-/-}$ DP T cells; Pearson's r, *Ets1-Fli1* expression correlation.

(C) Density histogram of smRNA-FISH *Ets1* mRNA in wild-type (gray) and *Gm27162*$^{-/-}$ (orange) DP T cells.

(D) Workflow for sequential smRNA FISH followed by ORCA imaging of the *Fli1* promoter (walk 10), *Ets1* promoter (walk 15), and *Gm27162* (walk 22; or *Gm27162* DFR in *Gm27162*$^{-/-}$ cells) in the same cells.

(E) Representative composite of overlaid smRNA FISH (*Fli1* mRNA, cyan; *Ets1* mRNA, red; DAPI, blue) and ORCA (fiducial, yellow; readout, red) images. Scale bar, 5 μm.

(F) Violin plots of *Ets1* (left) and *Fli1* (right) mRNA across wild-type (gray) and *Gm27162*$^{-/-}$ (orange) DP T cells (two-sided Wilcoxon rank-sum test).

(G) Violin plots of *Ets1* mRNA in wild-type and *Gm27162*$^{-/-}$ DP T cells grouped by *Ets1*-promoter interaction state. Two-sided Wilcoxon rank-sum test against the non-interacting cluster.

(H) Pie charts of *Ets1*-high (>25 mRNA molecules) wild-type and *Gm27162*$^{-/-}$ DP T cells binned by interaction group: (1) none (gray), (2) *Ets1-Fli1* promoter (blue), (3) *Ets1-Gm27162* (orange), and (4) three-way interaction (purple).

(I) Density histogram of *Ets1-Fli1* promoter distance (50-nm bins) in *Fli1*-high wild-type and *Gm27162*$^{-/-}$ DP T cells; dashed line, genotype mean; Pearson's r, *Ets1-Fli1* expression correlation.

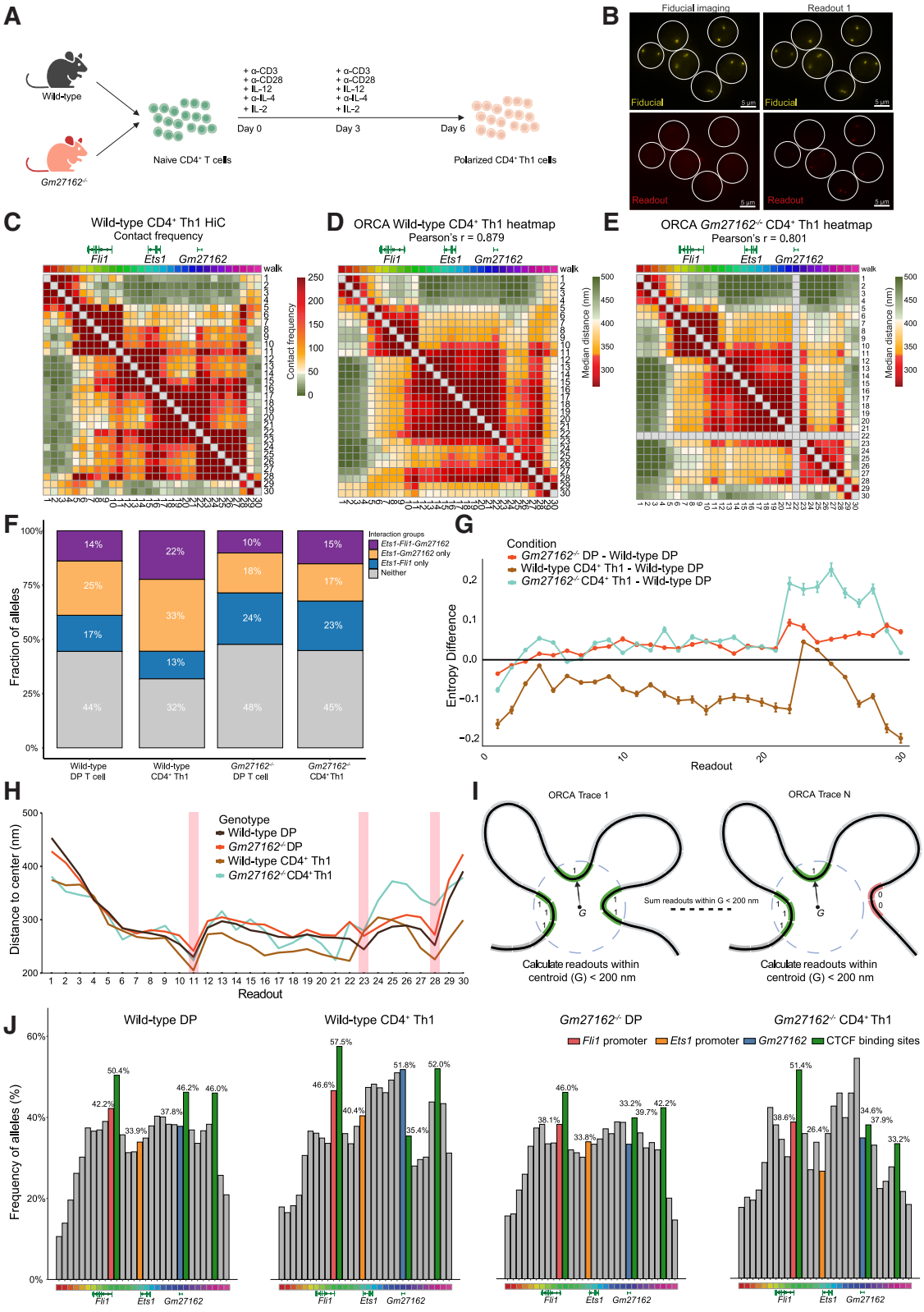


Figure 6. Th1 polarization repositions *Gm27162* super-enhancer to the center of the *Ets1-Fli1* locus

(A) Schematic of naive CD4$^+$ T cell isolation and Th1 polarization from wild-type and *Gm27162*$^{-/-}$ mice.

(B) Representative ORCA images (fiducial and readout) of wild-type CD4$^+$ Th1 cells; white circles, cell boundaries. Scale bar, 5 μm.

(legend continued on next page)

strongly with HiC contact-frequency map in relevant genotype (r = 0.879 and r = 0.801, Figures 6C–6E).

Th1 polarization increases multi-way interactions at the *Ets1-Fli1* locus

Pairwise interaction maps by bulk HiC or ensemble ORCA in Th1 cells preserved the architectural features observed in DP T cells (Figure 6C). The fraction of cells exhibiting *Ets1-Gm27162* interactions was higher in CD4$^+$ Th1 cells than in DP T cells, increasing from 25% to 33% (Figure 6F). This observation was supported by a decreased local radius of gyration within the *Ets1-Gm27162* domain, suggesting a more compact chromatin architecture between *Ets1* and its super-enhancer in CD4$^+$ Th1 cells relative to DP T cells (Figures S5D and S5E). Multi-way interactions among *Ets1*, *Fli1*, and *Gm27162* rose from 14% in DP T cells to 22% in CD4$^+$ Th1 cells. Interactions exclusively between *Ets1* and *Fli1* were limited in both cell types (17% and 13%, Figure 6F). Thus, cytokine stimulation modulated interaction preferences within the *Ets1-Fli1* locus, creating an interaction network distinct from DP T cells.

We next assessed how *Gm27162* loss reshaped the *Ets1-Fli1* locus in CD4$^+$ Th1 cells (Figure 6F). *Gm27162*$^{-/-}$ CD4$^+$ Th1 cells exhibited a 16% reduction in *Ets1-Gm27162* interactions and a 7% reduction in three-way interactions compared with wild-type CD4$^+$ Th1 cells (Figures 6F and S5F). Similar to DP T cells, we found a 10% increase in chromatin traces that engaged *Ets1-Fli1* contact exclusively in *Gm27162*$^{-/-}$ Th1 cells compared with wild-type counterparts. Strikingly, the interaction profile between the 3 elements in *Gm27162*$^{-/-}$ CD4$^+$ Th1 cells was quantitatively similar to *Gm27162*$^{-/-}$ DP T cells. We also computed entropy to assess the stability of chromatin conformations and found a more stable chromatin conformation in CD4$^+$ Th1 cells relative to DP T cells from wild-type mice (Figure 6G). Moreover, *Gm27162*$^{-/-}$ CD4$^+$ Th1 cells showed increased chromatin disorder, mirroring the entropy profile of *Gm27162*$^{-/-}$ DP T cells. Collectively, in the absence of *Gm27162*, the *Ets1-Fli1* locus in CD4$^+$ Th1 cells retained a DP T cell-like chromatin interaction profile, indicating that loss of *Gm27162* rendered the locus refractory to Th1-polarizing cytokine signaling.

Th1 polarization repositions the super-enhancer to the geometric center

Recent chromatin tracing studies by us[32] and others[33] suggest that radial positioning of enhancers can lead to transcriptional activation. To this end, we assessed if any elements were radially positioned within the *Ets1-Fli1* locus. We first computed the distance of each readout from the geometric center (or centroid) of each chromatin trace and plotted the average distance across all traces (Figure 6H). As reported,[34] CTCF binding sites in DP T cells localized proximally to the geometric center (pink bars, Figure 6H). However, in CD4$^+$ Th1 cells, the CTCF binding site -+245 kbp downstream of the *Ets1* promoter showed reduced propensity to localize to the geometric center. Instead, *Gm27162* super-enhancer was positioned more proximally to the geometric center in wild-type CD4$^+$ Th1 cells (Figure 6H).

Providing an independent approach to test radial positioning, we next quantified the proportion of chromatin traces where each genomic region was centrally positioned within the trace. We first defined the geometric center for each trace. Using a 200 nm interaction-distance threshold, we classified readouts within this radius as centrally positioned and plotted their frequency across all traces (Figure 6I). The super-enhancer *Gm27162* was centrally positioned within the *Ets1-Fli1* locus in 51.8% of wild-type CD4$^+$ Th1 cells, representing an increase over the 37.8% in DP T cells (Figure 6J). Representative chromatin traces from CD4$^+$ Th1 cells showed the central localization of *Gm27162* in addition to its interaction with the *Ets1* and *Fli1* promoters (Figure S5G). Extending this analysis to *Gm27162*$^{-/-}$ mice, we found comparable frequencies of traces maintaining the *Gm27162* DFR within the geometric center in CD4$^+$ Th1 and DP T cells (34.6% and 33.2%, Figure 6J). Thus, the *Gm27162* super-enhancer repositioned toward the geometric center of the *Ets1-Fli1* locus in response to cytokine stimulation in Th1 cells.

Combined RNA-DNA FISH in Th1 cells confirms the role of multi-way interaction in gene regulation

We next examined the regulation of *Ets1* and *Fli1* transcription in Th1 cells using combined RNA-DNA FISH. Median *Ets1* expression was higher in CD4$^+$ Th1 cells compared with DP T cells of wild-type mice (20 versus 17; Figures 7A and S6A), and a similar increase was observed for *Fli1* (14 versus 10; Figures 7A and S6B). In the absence of *Gm27162*, transcription of both genes was reduced (Figure 7A). To quantify paralog co-expression, we calculated the ratio of *Ets1* to *Fli1* mRNA counts per cell and determined the corresponding $\log_2$ fold change between the two transcripts. Wild-type CD4$^+$ Th1 cells exhibited greater *Ets1-Fli1* co-expression, whereas DP T cells showed a bias toward higher *Ets1* relative to *Fli1* expression (Figure 7B). In *Gm27162*$^{-/-}$ DP T cells, co-expression increased relative to both wild-type DP and Th1 cells, with a mean $\log_2$ fold change approaching zero. Similarly, *Gm27162*$^{-/-}$ CD4$^+$ Th1 cells showed enhanced co-expression, with a small negative mean $\log_2$ fold change indicating that, in some cells, *Fli1* expression exceeded that of *Ets1* (Figure 7B). Together, *Ets1*:*Fli1* ratio

(C) HiC contact-frequency heatmap of wild-type CD4$^+$ Th1 cells.
(D and E) ORCA median-distance heatmaps of pooled (D) wild-type and (E) *Gm27162*$^{-/-}$ CD4+ Th1 cell traces; Pearson's r, correlation with the wild-type and *Gm27162*$^{-/-}$ HiC matrices.
(F) Stacked bar plot of the fraction (%) of traces engaged in *Ets1-Fli1-Gm27162* three-way (purple), *Ets1-Gm27162* (orange), *Ets1-Fli1* (blue), or no (gray) interactions across the four cell types (wild-type and *Gm27162*$^{-/-}$ DP and CD4$^+$ Th1 cells).
(G) Per-readout entropy difference for *Gm27162*$^{-/-}$ DP (red), wild-type CD4$^+$ Th1 (brown), and *Gm27162*$^{-/-}$ CD4$^+$ Th1 (teal) cells relative to wild-type DP T cells.
(H) Mean per-readout distance from the geometric center of each trace for the four cell types (wild-type DP, black; *Gm27162*$^{-/-}$ DP, red; wild-type CD4$^+$ Th1, brown; *Gm27162*$^{-/-}$ CD4$^+$ Th1, teal); pink bars, CTCF-binding-site readouts (11, 23, and 28; −100 kbp, +245 kbp, and +390 kbp from the *Ets1* promoter).
(I) Schematic of quantifying readouts within 200 nm of the geometric center per trace; readouts labeled 1 (green) pass and 0 (red) fail the threshold.
(J) Bar charts of the frequency of traces for each readout within 200 nm of the geometric center. Base color bar, *Fli1*, *Ets1*, and *Gm27162* positions; green bars, CTCF binding sites (readouts 11, 23, and 28); red, orange, and blue bars, the *Fli1* promoter, *Ets1* promoter, and *Gm27162* (or DFR); percentages, frequency.

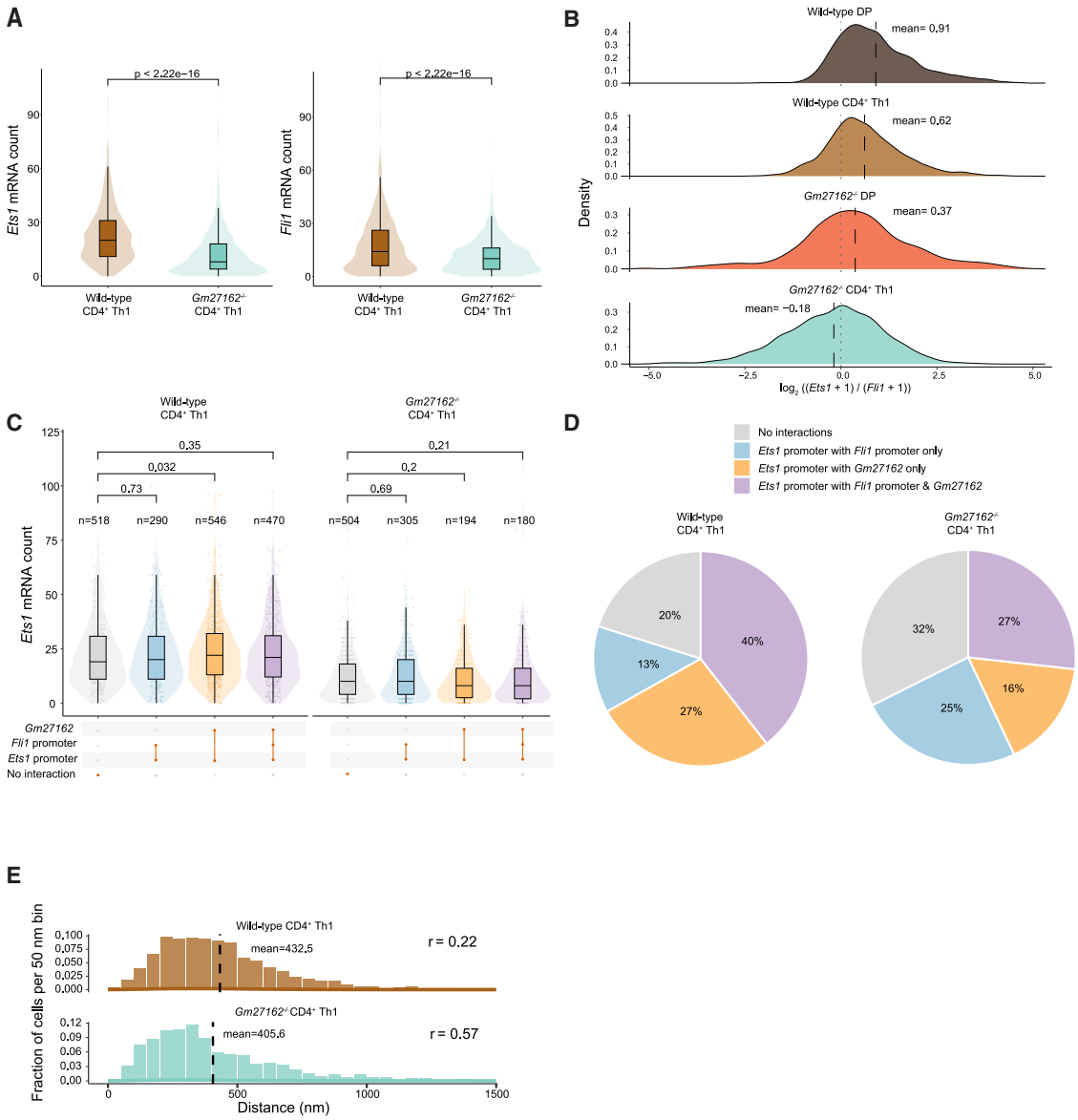


Figure 7. CD4$^+$ Th1 cells co-express *Ets1* and *Fli1* to a higher degree than DP T cells

(A) Violin plot of *Ets1* and *Fli1* smRNA-FISH spots in wild-type (brown) and *Gm27162*$^{-/-}$ (teal) CD4$^+$ Th1 cells, two-sided Wilcoxon rank-sum test.

(B) Density plot of the $\log_2$ fold change in the *Ets1*:*Fli1* mRNA ratio across the four cell types (wild-type DP, brown; wild-type CD4$^+$ Th1, light tan; *Gm27162*$^{-/-}$ DP, red; *Gm27162*$^{-/-}$ CD4$^+$ Th1, teal); dashed line, mean per cell type.

(C) Violin plots of *Ets1* mRNA grouped by *Ets1*-promoter interaction state as in Figure 5G for wild-type and *Gm27162*$^{-/-}$ CD4$^+$ Th1 cells, two-sided Wilcoxon rank-sum test.

(D) Pie charts of *Ets1*-high (>25 mRNA molecules) binned by interaction group for wild-type and *Gm27162*$^{-/-}$ CD4$^+$ Th1 cells.

(E) Density histogram of *Ets1*-*Fli1* promoter distance (50 nm bins) in *Fli1*-high wild-type (brown) and *Gm27162*$^{-/-}$ (teal) CD4$^+$ Th1 cells.

differed between DP and Th1 cells, consistent with their distinct chromatin architectures.

To assess which chromatin organization corresponded to the highest *Ets1* and *Fli1* levels in Th1 cells, we clustered Th1 cells based on their chromatin interaction states (Figure 7C). Wild-type CD4$^+$ Th1 cells expressed the highest level of *Ets1* mRNA when the *Ets1* promoter and *Gm27162* interacted (median = 22, Figure 7C). *Gm27162*$^{-/-}$ CD4$^+$ Th1 cells exhibited significant reduction in *Ets1* mRNA production across all interaction states (Figure 7C). Similar to the analysis in DP T cells, we quantified the proportion of *Ets1*^{high} cells (i.e., *Ets1* expression > 25 molecules) within each interaction category (Figure 7D). In wild-type Th1 cells, 66% of *Ets1*^{high} cells either had the *Ets1* promoter interacting with *Gm27162* exclusively or in combination with *Fli1* as a multi-way hub. In comparison with wild-type DP T cells, there was a 9% increase in *Ets1*^{high} cells driven as a multi-way hub in Th1 cells. *Ets1*^{high} cells driven by *Ets1*-*Fli1* promoter-promoter contacts were restricted to 13% of wild-type Th1 cells (Figure 7D). Extending beyond thresholding of *Ets1* expression, stratification of cells by graded *Ets1* mRNA abundance further

corroborated the association between high transcriptional output and preferential *Ets1-Gm27162* proximity (Figure S6C). Next, we explored *Fli1* expression differences within the *Fli1* promoter interaction clusters and found reduced expression of *Fli1* in *Gm27162*$^{-/-}$ Th1 cells across all clusters (Figure S6D). Analyzing the distribution of distances between *Ets1* and *Fli1* in *Fli1*^{high} Th1 cells suggested reduced distance between two promoters in the absence of *Gm27162* in agreement with DP T cells (Figure 7E versus 5I). *Gm27162*$^{-/-}$ CD4^{+} Th1 cells exhibited a stronger correlation in mRNA production associated with a reduced mean distance between the two loci, although each gene was also less transcribed (Figures 7E and 5I). Together, multi-way interactions in Th1 cells increased compared with DP T cells, and this arrangement correlated with the increased expression of both *Ets1* and *Fli1* in differentiated CD4^{+} T cells.

DISCUSSION

Comparison of chromatin tracing measurements in DP T cells and CD4^{+} Th1 cells suggests that cytokine signaling and TCR activation can influence local chromatin architecture at the *Ets1-Fli1* locus. The direct outcome of these extracellular cues was the selective repositioning of *Gm27162* super-enhancer toward the geometric center in CD4^{+} Th1 cells. *Gm27162* localization to the geometric center could increase its probability to encounter the *Ets1* promoter, possibly in a CTCF- and cohesin-dependent manner, thereby increasing the proportion of cells engaging in *Ets1-Gm27162* and cooperative *Ets1-Fli1-Gm27162* interactions. Alternatively, the radial repositioning of the super-enhancer may reflect its preferential association with transcriptional condensates that assemble under Th1 conditions and are spatially concentrated near the geometric center of the locus. Additional experiments are required to further evaluate these possibilities. Prior work using population-based sequencing assays suggests that 3D chromatin organization plays a key role in the co-regulation of type 2 cytokine genes *Il4*, *Il5*, and *Il13*.[14] Chromatin looping pre-configures the interactions between these three genes in naive CD4^{+} T cells, but transcription is restricted until Th2 polarization, which repositions the locus control region (LCR) within the *Rad50* intron closer to the promoters of the three genes in a STAT6 and Gata3 dependent manner.[14] We postulate that the geometric center of the *Il4-Il5-Il13* locus can also serve as the site facilitating interactions between the three genes as well as the LCR directing its expression in the context of Th2-polarizing cytokines. This concept could be generalized to other cytokine-responsive loci.

What accounts for the apparent resilience of early T cell development but the selective defect in CD4^{+} Th1 differentiation observed in *Gm27162*$^{-/-}$ mice? There are two possible explanations for this observation. The first explanation is the difference in baseline expression of *Ets1* and *Fli1* between DP T cells and CD4^{+} Th1 cells, where the latter expresses both genes to a significantly greater extent. According to ImmGen data,[35] throughout T cell development, there is a gradual increase in *Ets1* expression from the DN1 up to DP T cells, which express the highest level of *Ets1* in the thymus. When the locus is perturbed in *Gm27162*$^{-/-}$ mice, our data suggest that *Ets1* expression mediated by the *Ets1-Fli1* promoter-promoter interaction is adequate to sustain the expression requirements of early thymocyte development. CD4^{+} Th1 cells, however, increase the expression of *Ets1* and *Fli1* above the DP T cell threshold, and we believe that this elevated requirement of *Ets1* and *Fli1* cannot be sustained by reorganization of the genome in *Gm27162*$^{-/-}$ mice. An alternative yet concurrent possibility is the difference in chromatin interactions, which DP T cells and CD4^{+} Th1 cells engage in. A higher proportion of CD4^{+} Th1 cells engage in multi-way interactions including the *Ets1-Fli1* promoters and *Gm27162* super-enhancer. Th1 polarization may rely on these multi-way interactions through the radial positioning of *Gm27162* for transcriptional control of both genes rather than exclusivity between *Ets1-Gm27162*, which is most dominant in DP T cells. In *Gm27162*$^{-/-}$ mice, we suspect that the failure to remodel the locus due to cytokine signaling also hampers the ability of the *Ets1* promoter to find the *Fli1* promoter, thereby reducing the frequency of forming compensatory interactions sustaining *Ets1* and *Fli1* expression. Together, our data may suggest that the *Fli1* promoter is more utilized in the transcriptional control of CD4^{+} Th1 cells in wild-type mice, thereby restricting its compensatory roles in *Gm27162*$^{-/-}$ mice. Although we did not model the precise human sequence variants in individuals carrying disease-associated single-nucleotide polymorphisms (SNPs) at the *Ets1-Fli1* locus, genetic perturbation of the super-enhancer may disrupt its spatial positioning and multi-way promoter interactions in *cis*, thereby altering paralog expression and increasing susceptibility to CD4^{+} T cell-mediated immune disorders.

Limitations of the study

For the experiments combining RNA imaging with ORCA, we imaged mRNA for both *Ets1* and *Fli1* while detecting the *Ets1-Fli1* locus in both alleles. Generating distance measurements between *Ets1*, *Fli1*, and *Gm27162* from both alleles per cell limited the power of clustering chromatin traces into the four different interaction clusters since both allele distances equated to the same mRNA count per cell. Measuring nascent RNA expression of the two paralogs using intronic transcripts can help overcome this limitation and may assist with better quantification of allele-specific contribution to the expression of *Ets1* and *Fli1*. However, intronic RNA signals are inherently transient and reflect only active transcription sites at a given time point, which may lead to underestimation of total transcriptional output and even more increased variability in allele-specific measurements. Future experiments performing mRNA and intronic RNA side by side within the same cells will allow direct comparison of these approaches and help determine which method provides more accurate and robust quantification of allele-specific expression.

RESOURCE AVAILABILITY

Lead contact

Requests for reagents should be directed to, and will be fulfilled by, the lead contact, Golnaz Vahedi (vahedi@pennmedicine.upenn.edu).

Materials availability

Requests for mice generated in this study should be directed to the lead contact.

Data and code availability

The generated next-generation sequencing datasets are available in the Gene Expression Omnibus (GEO) repository under accession numbers GSE295630 and GSE295629. We generated a GitHub page for our study providing all scripts and imaging data, which were used for the analysis of this manuscript. All code and required data are deposited on GitHub and available at the following link: https://github.com/Atishayjay/single_allele_chromatin_tracing_Ets1_Fli1/.

ACKNOWLEDGMENTS

We thank Drs. Alistair Boettiger, Ting Wu, Guy Nir, and members of the Vutara VXL Slack group for their help with troubleshooting microfluidics and microscopy experiments. We are grateful to Katie Lupo for critical technical support. We thank members of the Vahedi and Faryabi laboratories, in particular Tobias, Panbeh, and Meshki. The work in this manuscript was supported by the NIH grants R01AI168136 (J. H.-M. and G.V.) and R01CA248041 (R.B.F.).

AUTHOR CONTRIBUTIONS

Conceptualization, A.J. and G.V.; methodology, A.J., Y.Z., B.N.A., M.F.M., A.C., S.Y., R.B.F., and G.V.; investigation, A.J. and G.V.; formal analysis, A.J. and S.Y.; resources and reagents, A.R., J.W., M.F.M., J.H.-M., R.B.F., and G.V.; writing original draft, A.J. and G.V.; writing review and editing, A.J., Y.Z., R.B.F., and G.V.; funding acquisition, R.B.F. and G.V.; supervision, R.B.F. and G.V.

DECLARATION OF INTERESTS

The authors declare no competing interests.

DECLARATION OF GENERATIVE AI AND AI-ASSISTED TECHNOLOGIES IN THE WRITING PROCESS

The authors used Claude for minor rephrasing but reviewed and edited the article afterward. The authors take full responsibility for the content of the published article.

STAR★METHODS

Detailed methods are provided in the online version of this paper and include the following:

- KEY RESOURCES TABLE
- EXPERIMENTAL MODEL AND SUBJECT DETAILS
  - Mice
  - Mouse DP T cell extraction
  - $CD4^+$ T cell isolation and polarization
  - FACS for live stained $CD4^+$ Th1 cells
- METHOD DETAILS
  - Genomics and sequencing experiments
- QUANTIFICATION AND STATISTICAL ANALYSIS
  - Statistical analysis
  - Preprocessing and spot registration
  - RNA FISH – ORCA cell registration
  - Contact threshold determination
  - Contact between *Fli1*, *Ets1* and *Gm27162*
  - Acetylated-methylated domain contacts
  - Radius of Gyration (R_g)
  - Acetylated-methylated domain compaction
  - Compaction between *Fli1* and *Ets1*
  - Compaction between *Ets1* and *Gm27162*
  - Entropy
  - Radial position trace clustering
  - Interaction-based allele clustering
  - *Ets1*/*Fli1* mRNA $\log_2$ (fold change)

SUPPLEMENTAL INFORMATION

Supplemental information can be found online at https://doi.org/10.1016/j.immuni.2026.08.001.

Received: May 29, 2025
Revised: March 5, 2026
Accepted: August 1, 2026
Published: August 24, 2026

REFERENCES

1. Vahedi, G., Kanno, Y., Sartorelli, V., and O'Shea, J.J. (2013). Transcription factors and CD4 T cells seeking identity: masters, minions, setters and spikers. Immunology *139*, 294–298. https://doi.org/10.1111/imm.12113.
2. Jay, A., Pondevida, C.M., and Vahedi, G. (2025). The epigenetic landscape of fate decisions in T cells. Nat. Immunol. *26*, 544–556. https://doi.org/10.1038/s41590-025-02113-x.
3. Shih, H.Y., Sciumè, G., Mikami, Y., Guo, L., Sun, H.W., Brooks, S.R., Urban, J.F., Jr., Davis, F.P., Kanno, Y., and O'Shea, J.J. (2016). Developmental Acquisition of Regulomes Underlies Innate Lymphoid Cell Functionality. Cell *165*, 1120–1133. https://doi.org/10.1016/j.cell.2016.04.029.
4. Thakore, P.I., Schnell, A., Huang, L., Zhao, M., Hou, Y., Christian, E., Zaghouani, S., Wang, C., Singh, V., Singaraju, A., et al. (2024). BACH2 regulates diversification of regulatory and proinflammatory chromatin states in TH17 cells. Nat. Immunol. *25*, 1395–1410. https://doi.org/10.1038/s41590-024-01901-1.
5. Gamble, N., Bradu, A., Caldwell, J.A., McKeever, J., Bolonduro, O., Ermis, E., Kaiser, C., Kim, Y., Parks, B., Klemm, S., et al. (2024). PU.1 and BCL11B sequentially cooperate with RUNX1 to anchor mSWI/SNF to poise the T cell effector landscape. Nat. Immunol. *25*, 860–872. https://doi.org/10.1038/s41590-024-01807-y.
6. Vahedi, G., Kanno, Y., Furumoto, Y., Jiang, K., Parker, S.C., Erdos, M.R., Davis, S.R., Roychoudhuri, R., Restifo, N.P., Gadina, M., et al. (2015). Super-enhancers delineate disease-associated regulatory nodes in T cells. Nature *520*, 558–562. https://doi.org/10.1038/nature14154.
7. Vahedi, G., Takahashi, H., Nakayamada, S., Sun, H.W., Sartorelli, V., Kanno, Y., and O'Shea, J.J. (2012). STATs shape the active enhancer landscape of T cell populations. Cell *151*, 981–993. https://doi.org/10.1016/j.cell.2012.09.044.
8. Ciofani, M., Madar, A., Galan, C., Sellars, M., Mace, K., Pauli, F., Agarwal, A., Huang, W., Parkhurst, C.N., Muratet, M., et al. (2012). A validated regulatory network for Th17 cell specification. Cell *151*, 289–303. https://doi.org/10.1016/j.cell.2012.09.016.
9. Ostuni, R., Piccolo, V., Barozzi, I., Polletti, S., Termanini, A., Bonifacio, S., Curina, A., Prosperini, E., Ghisletti, S., and Natoli, G. (2013). Latent enhancers activated by stimulation in differentiated cells. Cell *152*, 157–171. https://doi.org/10.1016/j.cell.2012.12.018.
10. Ramirez-Carrozzi, V.R., Braas, D., Bhatt, D.M., Cheng, C.S., Hong, C., Doty, K.R., Black, J.C., Hoffmann, A., Carey, M., and Smale, S.T. (2009). A unifying model for the selective regulation of inducible transcription by CpG islands and nucleosome remodeling. Cell *138*, 114–128. https://doi.org/10.1016/j.cell.2009.04.020.
11. Wei, G., Wei, L., Zhu, J., Zang, C., Hu-Li, J., Yao, Z., Cui, K., Kanno, Y., Roh, T.Y., Watford, W.T., et al. (2009). Global mapping of H3K4me3 and H3K27me3 reveals specificity and plasticity in lineage fate determination of differentiating CD4+ T cells. Immunity *30*, 155–167. https://doi.org/10.1016/j.immuni.2008.12.009.
12. Shi, M., Lin, T.H., Appell, K.C., and Berg, L.J. (2008). Janus-kinase-3-dependent signals induce chromatin remodeling at the Ifng locus during T helper 1 cell differentiation. Immunity *28*, 763–773. https://doi.org/10.1016/j.immuni.2008.04.016.
13. Cui, K., Chen, Z., Cao, Y., Liu, S., Ren, G., Hu, G., Fang, D., Wei, D., Liu, C., Zhu, J., et al. (2023). Restraint of IFN-gamma expression through a distal

silencer CNS-28 for tissue homeostasis. Immunity *56*, 944–958.e6. https://doi.org/10.1016/j.immuni.2023.03.006.

14. Nagashima, H., Shayne, J., Jiang, K., Petermann, F., Pękowska, A., Kanno, Y., and O'Shea, J.J. (2024). Remodeling of Il4-Il13-Il5 locus underlies selective gene expression. Nat. Immunol. *25*, 2220–2233. https://doi.org/10.1038/s41590-024-02007-4.
15. Garrett-Sinha, L.A. (2013). Review of Ets1 structure, function, and roles in immunity. Cell. Mol. Life Sci. *70*, 3375–3390. https://doi.org/10.1007/s00018-012-1243-7.
16. Ben-David, Y., Gajendran, B., Sample, K.M., and Zacksenhaus, E. (2022). Current insights into the role of Fli-1 in hematopoiesis and malignant transformation. Cell. Mol. Life Sci. *79*, 163. https://doi.org/10.1007/s00018-022-04160-1.
17. Garrett-Sinha, L.A. (2023). An update on the roles of transcription factor Ets1 in autoimmune diseases. WIREs Mech. Dis. *15*, e1627. https://doi.org/10.1002/wsbm.1627.
18. Chandra, A., Yoon, S., Michieletto, M.F., Goldman, N., Ferrari, E.K., Abedi, M., Johnson, I., Fasolino, M., Pham, K., Joannas, L., et al. (2023). Quantitative control of Ets1 dosage by a multi-enhancer hub promotes Th1 cell differentiation and protects from allergic inflammation. Immunity *56*, 1451–1467.e12. https://doi.org/10.1016/j.immuni.2023.05.004.
19. Mateo, L.J., Sinnott-Armstrong, N., and Boettiger, A.N. (2021). Tracing DNA paths and RNA profiles in cultured cells and tissues with ORCA. Nat. Protoc. *16*, 1647–1713. https://doi.org/10.1038/s41596-020-00478-x.
20. Bintu, B., Mateo, L.J., Su, J.H., Sinnott-Armstrong, N.A., Parker, M., Kinrot, S., Yamaya, K., Boettiger, A.N., and Zhuang, X. (2018). Super-resolution chromatin tracing reveals domains and cooperative interactions in single cells. Science *362*, eaau1783. https://doi.org/10.1126/science.aau1783.
21. Hafner, A., Park, M., Berger, S.E., Murphy, S.E., Nora, E.P., and Boettiger, A.N. (2023). Loop stacking organizes genome folding from TADs to chromosomes. Mol. Cell *83*, 1377–1392.e6. https://doi.org/10.1016/j.molcel.2023.04.008.
22. Le, D.J., Hafner, A., Gaddam, S., Wang, K.C., and Boettiger, A.N. (2024). Super-enhancer interactomes from single cells link clustering and transcription. Preprint at bioRxiv, 2024.05.08.593251. https://doi.org/10.1101/2024.05.08.593251.
23. Murphy, S.E., and Boettiger, A.N. (2024). Polycomb repression of Hox genes involves spatial feedback but not domain compaction or phase transition. Nat. Genet. *56*, 493–504. https://doi.org/10.1038/s41588-024-01661-6.
24. Fasolino, M., Goldman, N., Wang, W., Cattau, B., Zhou, Y., Petrovic, J., Link, V.M., Cote, A., Chandra, A., Silverman, M., et al. (2020). Genetic Variation in Type 1 Diabetes Reconfigures the 3D Chromatin Organization of T Cells and Alters Gene Expression. Immunity *52*, 257–274.e11. https://doi.org/10.1016/j.immuni.2020.01.003.
25. Petrovic, J., Zhou, Y., Fasolino, M., Goldman, N., Schwartz, G.W., Mumbach, M.R., Nguyen, S.C., Rome, K.S., Sela, Y., Zapataro, Z., et al. (2019). Oncogenic Notch Promotes Long-Range Regulatory Interactions within Hyperconnected 3D Cliques. Mol. Cell *73*, 1174–1190.e12. https://doi.org/10.1016/j.molcel.2019.01.006.
26. Skene, P.J., and Henikoff, S. (2017). An efficient targeted nuclease strategy for high-resolution mapping of DNA binding sites. eLife *6*, e21856. https://doi.org/10.7554/eLife.21856.
27. Lieberman-Aiden, E., van Berkum, N.L., Williams, L., Imakaev, M., Ragoczy, T., Telling, A., Amit, I., Lajoie, B.R., Sabo, P.J., Dorschner, M.O., et al. (2009). Comprehensive mapping of long-range interactions reveals folding principles of the human genome. Science *326*, 289–293. https://doi.org/10.1126/science.1181369.
28. Rao, S.S., Huntley, M.H., Durand, N.C., Stamenova, E.K., Bochkov, I.D., Robinson, J.T., Sanborn, A.L., Machol, I., Omer, A.D., Lander, E.S., et al. (2014). A 3D map of the human genome at kilobase resolution reveals principles of chromatin looping. Cell *159*, 1665–1680. https://doi.org/10.1016/j.cell.2014.11.021.
29. Boettiger, A.N., Bintu, B., Moffitt, J.R., Wang, S., Beliveau, B.J., Fudenberg, G., Imakaev, M., Mirny, L.A., Wu, C.T., and Zhuang, X. (2016). Super-resolution imaging reveals distinct chromatin folding for different epigenetic states. Nature *529*, 418–422. https://doi.org/10.1038/nature16496.
30. Mirny, L.A. (2011). The fractal globule as a model of chromatin architecture in the cell. Chromosome Res. *19*, 37–51. https://doi.org/10.1007/s10577-010-9177-0.
31. Phanstiel, D.H., Boyle, A.P., Araya, C.L., and Snyder, M.P. (2014). Sushi.R: flexible, quantitative and integrative genomic visualizations for publication-quality multi-panel figures. Bioinformatics *30*, 2808–2810. https://doi.org/10.1093/bioinformatics/btu379.
32. Zhou, Y., Jay, A., Burget, N., Friedrich, T., Yoon, S., Alsing, J., Nir, G., Grosschedl, R., Vahedi, G., and Faryabi, R.B. (2026). Lineage-determining transcription factors constrain cohesin to drive multi-enhancer oncogene regulation. Nat. Cell Biol. *28*, 149–165. https://doi.org/10.1038/s41556-025-01827-2.
33. Bohrer, C.H., and Larson, D.R. (2023). Synthetic analysis of chromatin tracing and live-cell imaging indicates pervasive spatial coupling between genes. eLife *12*, e81861. https://doi.org/10.7554/eLife.81861.
34. Hung, T.C., Kingsley, D.M., and Boettiger, A.N. (2024). Boundary stacking interactions enable cross-TAD enhancer-promoter communication during limb development. Nat. Genet. *56*, 306–314. https://doi.org/10.1038/s41588-023-01641-2.
35. Heng, T.S., and Painter, M.W.; Immunological Genome Project Consortium (2008). The Immunological Genome Project: networks of gene expression in immune cells. Nat. Immunol. *9*, 1091–1094. https://doi.org/10.1038/ni1008-1091.
36. Team, R.C. (2021). R: a Language and Environment for Statistical Computing (R Foundation for Statistical Computing).
37. Van Rossum, G., and Drake, F.L. (2009) Python 3 Reference Manual (CreateSpace).
38. Andrews, S. (2010). FastQC: A Quality Control Tool for High Throughput Sequence Data.
39. Krueger, F. (2021). Trimgalore.
40. Li, H., and Durbin, R. (2009). Fast and accurate short read alignment with Burrows-Wheeler transform. Bioinformatics *25*, 1754–1760. https://doi.org/10.1093/bioinformatics/btp324.
41. Institute, B. (2021). Picard Toolkit (Broad Institute, GitHub Repository).
42. Zhang, Y., Liu, T., Meyer, C.A., Eeckhoute, J., Johnson, D.S., Bernstein, B.E., Nusbaum, C., Myers, R.M., Brown, M., Li, W., et al. (2008). Model-based analysis of ChIP-Seq (MACS). Genome Biol. *9*, R137. https://doi.org/10.1186/gb-2008-9-9-r137.
43. Ramírez, F., Dündar, F., Diehl, S., Grüning, B.A., and Manke, T. (2014). deepTools: a flexible platform for exploring deep-sequencing data. Nucleic Acids Res. *42*, W187–W191. https://doi.org/10.1093/nar/gku365.
44. Servant, N., Varoquaux, N., Lajoie, B.R., Viara, E., Chen, C.J., Vert, J.P., Heard, E., Dekker, J., and Barillot, E. (2015). HiC-Pro: an optimized and flexible pipeline for Hi-C data processing. Genome Biol. *16*, 259. https://doi.org/10.1186/s13059-015-0831-x.
45. Quinlan, A.R., and Hall, I.M. (2010). BEDTools: a flexible suite of utilities for comparing genomic features. Bioinformatics *26*, 841–842. https://doi.org/10.1093/bioinformatics/btq033.
46. Robinson, J.T., Thorvaldsdóttir, H., Winckler, W., Guttman, M., Lander, E.S., Getz, G., and Mesirov, J.P. (2011). Integrative genomics viewer. Nat. Biotechnol. *29*, 24–26. https://doi.org/10.1038/nbt.1754.
47. Niu, Z., Bruyère, T., Manthey, D., Li, J., O'Farrell, A., and Raj, A. (2026). NimbusImage: a cloud-computing platform for image analysis. Nat. Methods *23*, 6–8. https://doi.org/10.1038/s41592-025-02942-6.
48. Beliveau, B.J., Kishi, J.Y., Nir, G., Sasaki, H.M., Saka, S.K., Nguyen, S.C., Wu, C.T., and Yin, P. (2018). OligoMiner provides a rapid, flexible environment for the design of genome-scale oligonucleotide in situ hybridization probes. Proc. Natl. Acad. Sci. USA *115*, E2183–E2192. https://doi.org/10.1073/pnas.1714530115.

49. Abdennur, N., Abraham, S., Fudenberg, G., Flyamer, I.M., Galitsyna, A.A., Goloborodko, A., Imakaev, M., Oksuz, B.A., Venev, S.V., et al.; Open2C (2024). Cooltools: Enabling high-resolution Hi-C analysis in Python. PLOS Comput. Biol. *20*, e1012067. https://doi.org/10.1371/journal.pcbi.1012067.

50. Stringer, C., Wang, T., Michaelos, M., and Pachitariu, M. (2021). Cellpose: a generalist algorithm for cellular segmentation. Nat. Methods *18*, 100–106. https://doi.org/10.1038/s41592-020-01018-x.

51. Rigano, A., Ehmsen, S., Öztürk, S.U., Ryan, J., Balashov, A., Hammer, M., Kirli, K., Boehm, U., Brown, C.M., Bellve, K., et al. (2021). Micro-Meta App: an interactive tool for collecting microscopy metadata based on community specifications. Nat. Methods *18*, 1489–1495. https://doi.org/10.1038/s41592-021-01315-z.

52. Li, H., Handsaker, B., Wysoker, A., Fennell, T., Ruan, J., Homer, N., Marth, G., Abecasis, G., and Durbin, R.; 1000 Genome Project Data Processing Subgroup (2009). The Sequence Alignment/Map format and SAMtools. Bioinformatics *25*, 2078–2079. https://doi.org/10.1093/bioinformatics/btp352.

53. Aguilar, S.V., Aguilar, O., Allan, R., Amir, E.D., Angeli, V., Artyomov, M.N., Asinovski, N., Astarita, J., Austen, K.F., and Bajpai, G. (2020). ImmGen at 15. Nat. Immunol. *21*, 700–703. https://doi.org/10.1038/s41590-020-0687-4.

54. Schneider, C.A., Rasband, W.S., and Eliceiri, K.W. (2012). NIH Image to ImageJ: 25 years of image analysis. Nat. Methods *9*, 671–675. https://doi.org/10.1038/nmeth.2089.

55. Raj, A., van den Bogaard, P., Rifkin, S.A., van Oudenaarden, A., and Tyagi, S. (2008). Imaging individual mRNA molecules using multiple singly labeled probes. Nat. Methods *5*, 877–879. https://doi.org/10.1038/nmeth.1253.

STAR★METHODS

KEY RESOURCES TABLE

REAGENT or RESOURCE	SOURCE	IDENTIFIER
Antibodies		
Anti-mouse B220 (Clone: RA3-6B2) APC	BioLegend	Cat# 103211; RRID: AB_312996
Anti-mouse CD4 (Clone: RM4-4) PE	BioLegend	Cat# 116005; RRID: AB_313690
Anti-mouse CD8 (Clone:53-6.7) BV650	BioLegend	Cat# 100741; RRID: AB_11124344
Anti-mouse CD11b (Clone: M1/70) APC	BioLegend	Cat# 101212; RRID: AB_312795
Anti-mouse CD11c (Clone: N418) APC	BioLegend	Cat# 117309; RRID: AB_313778
Anti-mouse CD25 (Clone: PC61) PE/Cy7	BioLegend	Cat# 102015; RRID: AB_312864
Anti-mouse CD44 (Clone: IM7) BV785	BioLegend	Cat# 103059; RRID: AB_2571953
Anti-mouse TCRb (Clone: H57-597) APC	BioLegend	Cat# 109212; RRID: AB_313435
Anti-mouse TCRgd (Clone: GL3) APC	BioLegend	Cat# 118115; RRID: AB_1731824
Anti-mouse Ter119 (Clone: TER-119) APC	BioLegend	Cat# 116212; RRID: AB_313713
Anti-mouse IFNγ (Clone: XMG1.2) PerCP/Cyanine5.5	BioLegend	Cat# 505821; RRID: AB_961361
Anti-mouse Gr-1 (Clone: RB6-8C5) APC	BioLegend	Cat# 108411; RRID: AB_313376
Anti-mouse NK1.1 (Clone: PK136) APC	BioLegend	Cat# 108709; RRID: AB_313396
Anti-CD3ε Armenian Hamster Monoclonal Antibody (LEAF – Clone: 145-2C11)	BioLegend	Cat# 100302; RRID: AB_312667
Anti-CD28 Syrian Hamster Monoclonal Antibody (Clone: 37.51)	BD Biosciences	Cat# 553294; RRID: AB_394763
InVivoMab anti-mouse IL-4 (Clone: 11B11)	Bio X Cell	Cat# BE0045; RRID: AB_1107707
Anti-CTCF	Millipore	Cat# 07-729; RRID: AB_441965
Anti-Acetyl-Histone H3 (Lys27) (D5E4)	Cell Signaling Technology	Cat# 8173S; RRID: AB_10949503
H3K27me3 Antibody, SNAP-Certified™ for CUT&RUN and CUT&Tag	EpiCypher	Cat# 13-0055; RRID: AB_3665059
Chemicals, peptides, and recombinant proteins		
Recombinant IL-2 (mouse)	BioLegend	Cat# 575402
Recombinant IL-12 (mouse)	BioLegend	Cat# 577002
Viability Dye LIVE/DEAD™ Fixable Aqua Dead Cell Stain Kit	ThermoFisher Scientific	Cat# L34957
Fixable Viability Dye eFluor™ 780	ThermoFisher Scientific	Cat# 50-112-9035
Phorbol 12-myristate 13-acetate (PMA)	Sigma- Aldrich	Cat# P8139-1MG
Ionomycin calcium salt from Streptomyces conglobatus	Sigma- Aldrich	Cat# I0634-1MG
GolgiPlug Protein Transport Inhibitor	BD Biosciences	Cat# 555029
RPMI 1640 medium	Invitrogen	Cat# 11875085
Fetal Bovine Serum	Sigma- Aldrich	Cat# F2442
GemCell™ - Fetal Bovine Serum	Gemini Bio	Cat# 100-500, Lot# A03HOOK
2-Mercaptoethanol	Sigma	Cat# M6250-10ML
ACK Lysing Buffer	ThermoFisher Scientific	Cat# A1049201
HEPES	ThermoFisher	Cat# 15630080
Non-Essential Amino Acids	ThermoFisher	Cat# 11140050
Penicillin-Streptomycin	ThermoFisher	Cat# 15140122
Sodium Pyruvate	ThermoFisher	Cat# 11360070
L-Glutamine (200 mM)	ThermoFisher	Cat# 25030081
Formaldehyde solution 16%	Thermo	Cat# PI28908

(*Continued on next page*)

Continued

REAGENT or RESOURCE	SOURCE	IDENTIFIER
cOmplete™, EDTA-free Protease Inhibitor Cocktail	Roche	Cat# 11873580001
Qubit dsDNA HS Assay Kit	Invitrogen	Cat# Q32851
Phusion PCR Master Mix	NEB	Cat# M0531
Nextera XT Index Kit	Illumina	Cat# FC-131-1001
SPRIselect	Beckman Coulter	Cat# B2331
Polysine microscope slides	Thermo Scientific	Cat# P4981-001
Silicone isolators	Electron Microscopy Sciences	Cat# 70339-05
Ethanol	Decon Laboratories	Cat# 2716
Dimethylformamide	Sigma-Aldrich	Cat# D4551
Polyvinylsulfonic acid (PVSA)	Sigma Aldrich	Cat# 278424
Coverslips	Fisher Scientific	Cat# 12-548-5M
Nowrinkle rubber cement	Elmer's	N/A
Slowfade Gold Antifade Reagent	Invitrogen by Thermo Fisher Scientific	Cat# S36936
Dries instantly top coat	Sally Hansen's	Cat# 45114
Fixation/Permeabilization Solution Kit	BD Biosciences	Cat# 554714
Foxp3/ Transcription Factor Staining Buffer Set	Thermo	Cat# 00-5523-00
Ribonucleoside Vanadyl Complex	New England Biolabs	Cat# S1402S
RNasin® Plus Ribonuclease Inhibitor	Promega Corporation	Cat# N2615
RNase A, DNase and protease-free (10 mg/mL)	ThermoFisher	Cat# EN0531
Dextran sulfate sodium salt from Leuconostoc spp.	Millipore Sigma	Cat# D8906-50G
dNTP mixture, 100mM (25mM of each)	Thomas Scientific	Cat# C788T68
Glucose Oxidase	Fisher Scientific	Cat# G00501G
Catalase	Thomas Scientific	Cat# 210040280
D-(+)-Glucose	Fisher Scientific	Cat# AAA1682836
Formamide (Deionized)	Ambion	Cat# AM9344
Triton™ X-100	Millipore Sigma	Cat# T8787-250ML
Oligonucleotides		
ORCA primary oligos	Table S1	N/A
ORCA barcode oligos	Table S2	N/A
Stellaris smRNA-FISH probe set — *Ets1* mRNA (CAL Fluor Red 610)	Biosearch technologies	Cat# SMF-1082-5
Stellaris smRNA-FISH probe set — *Ets1* mRNA (Quasar 570)	Biosearch technologies	Cat# SMF-1063-5
Stellaris smRNA-FISH probe set — *Fli1* mRNA (Quasar 670)	Biosearch technologies	Cat# SMF-1065-5
Stellaris smRNA-FISH probe set — *Fli1* mRNA (Quasar 570)	Biosearch technologies	Cat# SMF-1063-5
Stellaris smRNA-FISH probe set — *Gapdh* mRNA (control – Quasar 670)	Biosearch technologies	Cat# SMF-3140-1
ORCA Fiducial probe: /5Cy3/ ATGTGGGCGCCCGAATAAAG/3Cy3Sp/	Integrated DNA Technologies	N/A
Secondary ORCA probe (odd barcodes): /5Alex647N/ GCGAATCCGACGCACCGCTA/ 3AlexF647N/	Integrated DNA Technologies	N/A

(*Continued on next page*)

Continued		
REAGENT or RESOURCE	SOURCE	IDENTIFIER
Secondary ORCA probe (even barcodes): /5Alex647N/ GGACCCTGTTCGGCTAACCA/ 3AlexF647N/	Integrated DNA Technologies	N/A
Critical commercial assays		
CUTANA™ ChIC/CUT&RUN Kit	EpiCypher	Cat# 14-1048
NEBNext Ultra II DNA Library Prep Kit for Illumina	NEB	Cat# E7645S
D1000 ScreenTape	Agilent	Cat# 5067-5582
D1000 Reagents	Agilent	Cat# 5067-5583
High Sensitivity D1000 ScreenTape	Agilent	Cat# 5067-5584
High Sensitivity D1000 Reagents	Agilent	Cat# 5067-5585
Genomic DNA ScreenTape	Agilent	Cat# 5067-5365
Genomic DNA Reagents	Agilent	Cat# 5067-5366
Arima HiC kit	Arima Genomics	N/A
Accel-NGS 2S Plus DNA Library Kit	Swift Biosciences	Cat# 21024
MinElute Reaction Cleanup Kit	QIAGEN	Cat# 28204
QIAQuick PCR Purification Kit	QIAGEN	Cat# 28104
EasySep™ Mouse Naïve $CD4^+$ T Cell Isolation Kit	StemCell	Cat# 19765
Deposited data		
HiC	This study	GEO: GSE295630
CUT&RUN	This study	GEO: GSE295629
Experimental models: Organisms/strains		
Mouse: C57BL/6J	Jackson Laboratories	RRID: IMSR_JAX:000664
Mouse: C57BL/6J-*Gm27162*$^{-/-}$	This study	N/A
Mouse: C57BL/6J-CBS +245kbp$^{-/-}$	This study	N/A
Software and algorithms		
R 4.1.1	R Core Team[36]	https://www.R-project.org/
Python 3.8	Van Rossum and Drake[37]	https://peps.python.org/pep-0569/
FastQC v0.11.9	Andrews[38]	http://www.bioinformatics.babraham.ac.uk/projects/fastqc/
Trim_Galore v0.6.6	Krueger[39]	https://github.com/FelixKrueger/TrimGalore
BWA v0.7.17-r1188	Li and Durbin[40]	https://bio-bwa.sourceforge.net
Picard v2.26.7	Broad Institute[41]	http://broadinstitute.github.io/picard/
MACS2 v2.1.4	Zhang et al.[42]	https://pypi.org/project/MACS2/2.1.4/
bamCoverage v3.3.2	Ramírez et al.[43]	https://deeptools.readthedocs.io/en/develop/content/tools/bamCoverage.html
HiC-Pro v2.8	Servant et al.[44]	https://github.com/nservant/HiC-Pro/
bedtools v2.30.0	Quinlan and Hall[45]	https://bedtools.readthedocs.io/en/latest/content/installation.html
Integrative Genome Browser v2.9.13	Robinson et al.[46]	https://software.broadinstitute.org/software/igv/
Sushi v1.28.0	Phanstiel[31]	http://bioconductor.riken.jp/packages/
Stellaris-probe-designer	Biosearch technologies	https://www.biosearchtech.com/support/tools/design-software/stellaris-probe-designer
NimbusImage	Niu et al.[47]	https://www.github.com/Kitware/UpennContrast

(*Continued on next page*)

Continued

REAGENT or RESOURCE	SOURCE	IDENTIFIER
Deeptools v3.5.1	Ramírez et al.[43]	https://deeptools.readthedocs.io/en/develop/
Oligominer	Beliveau et al.[48]	https://github.com/beliveau-lab/OligoMiner
Cooltools	Open2C et al.[49]	https://github.com/open2c/cooltools
Cellpose v.2.2.2	Stringer et al.[50]	N/A
ORCA ChrTracer3 spot caller	Mateo et al.[19]	https://github.com/BoettigerLab/ORCA-public
Vutara SRX v.7.3.22	Bruker Corporation	https://www.bruker.com/en/products-and-solutions/fluorescence-microscopy/super-resolution-microscopes/srx-software.html
MATLAB R2022a	MathWorks	https://www.mathworks.com/products/matlab.html
Torch v2.0.1	PyTorch	https://pytorch.org
Micro-Meta App	Rigano et al.[51]	https://github.com/WU-BIMAC/MicroMetaApp-docs
Samtools 1.11	LI et al.[52]	https://samtools.sourceforge.net
ImmGen	The Immunological Genome Project[53]	https://www.immgen.org
ImageJ	Schneider et al.[54]	https://imagej.net
FlowJo v10.8.2	TreeStar	https://www.flowjo.com/solutions/flowjo/downloads
GraphPad Prism 9 Version 9.5.1 (528), January 24, 2023	GraphPad Software	https://www.graphpad.com/scientific-software/prism/

EXPERIMENTAL MODEL AND SUBJECT DETAILS

Mice

The *Gm27162*$^{-/-}$ mice were generated using CRISPR/Cas9 system as previously described.[18] The CBS +245kbp$^{-/-}$ mice were generated using CRISPR/Cas9 with sgRNA sequences 5' TTTCTTGGGAGGTTTGCTAGAGG and 3' CCTCCTGTGTTGTGCTGCTAGGA targeting CTCF binding sites within the following DNA region referred to as CBS +245kbp: chr9:32,938,663-32,944,818 (mm10 genome). CBS +245kbp$^{-/-}$ mice were backcrossed onto the C57BL/6 background for at least three generations to control for potential off-target effects. Spleens and thymi from these mice were used for microscopy experiments respectively. All mice were bred and maintained under pathogen-free conditions at an American Association for the Accreditation of Laboratory Animal Care accredited animal facility at the University of Pennsylvania. Mice were housed in accordance with the procedures outlined in the Guide for the Care and Use of Laboratory Animals under an animal study proposal approved by an institutional Animal Care and Use Committee. All experiments were performed using 6- to 10-weeks old age and sex matched mice and using both males and females.

Mouse DP T cell extraction

Double positive T-cells were isolated by physical dissociation of the mouse thymus through a 70μm filter (Falcon) in RPMI 1640 medium (Invitrogen). Cells were spun down at 800xg for 5 min, resuspended in 10mL of RPMI 1640, and counted using a Countess cell counting chamber slide (Thermo Fisher Scientific). Following this, the cells were diluted to 6.6 million cells per mL. 300μL of the diluted cells were added to a poly-L-Lysine-coated 40mm coverslip (Bioptechs) and allowed to adhere for 1 hour at room temperature inside a humidified chamber. Cells were briefly washed in cold 1xPBS, fixed in 4% formaldehyde (Fisher Scientific, cat#PI28908) diluted in 1xPBS for 10 min and then washed twice with 1xPBS. Coverslips were stored in 60mm dishes (USAScientific, cat#8609-0160) filled with 10 mL of 1xPBS at 4°C or used immediately for ORCA hybridization.

CD4$^+$ T cell isolation and polarization

Splenocytes were isolated from the mouse spleen of wild-type and *Gm27162*$^{-/-}$ mice. Cells were first subjected to ACK lysis buffer (Gibco, Invitrogen) to remove red blood cells. Naïve CD4$^+$ T cells were enriched using negative selection beads (STEMCELL, Cat# 19765) following the manufacturer's recommendations. Cells were cultured in RPMI 1640 medium (Invitrogen), supplemented with 10% fetal bovine serum (Fisher Scientific), 1mM sodium pyruvate (Gibco), 1X GlutaMAX (Gibco), 10mM HEPES (Gibco), 1% penicillin-streptomycin, and 0.1% 2-Mercaptoethanol (Gibco). For *in vitro* polarization, flat-bottom 96-well plates were coated with 2 μg/mL of anti-CD3 (clone:145-2C11, BioLegend, Cat#100302) in PBS overnight at 4°C. For Th1 polarization, 0.2 × 10^6 naïve CD4$^+$ T cells were cultured in the presence of 10 ng/mL of recombinant IL-12 (BioLegend, Cat#577002), 1 ng/mL of recombinant IL-2 (BioLegend, Cat#575402), 10 μg /mL of soluble anti-IL-4 (Clone: 11B11, Bio X Cell, Cat# BE0045) and 1 μg /mL of soluble anti-CD28

(clone:37.51, BD Biosciences, Cat# 553294) for 6 days at 37°C. At day 3 post-stimulation, half of the medium was removed and replaced with fresh medium containing 2X cytokine concentration.

FACS for live stained CD4$^+$ Th1 cells

At day 6 under Th1 polarizing conditions, cells were stimulated with PMA, Ionomycin and Golgi Plug for 4 hours at 37°C. Subsequently, they were stained with a viability dye (1:1000, eFluor 780), washed with 1xPBS and then fixed in 4% PFA. Prior to sorting, cells were resuspended to a concentration of 10 x 10^6 cells/mL in 1xPBS supplemented with 2% BSA and filtered through a 70 μm filter. BD FACS Aria II was used to sort for eFluor 780 negative cells using a 100 μm filter. Cells were sorted into a 15 mL Falcon tube containing 1xPBS supplemented with 2% BSA.

METHOD DETAILS

Genomics and sequencing experiments

HiC

HiC libraries were generated as outlined in Chandra et al.[18] using 0.5 - 1x10^6 cells with Arima-HiC+ kit (Arima Genomics) and Accel-NGS 2S Plus DNA Library kit (21024 Swift Biosciences), according to the manufacturer's recommendations. Libraries were validated for quality and size distribution using Qubit dsDNA HS Assay Kit (Invitrogen, cat# Q32851) and TapeStation 2200 (Agilent). Libraries were paired-end sequenced (66bp+66bp) on NovaSeq 6000 (Illumina).

HiC analysis

HiC alignment and triangle heatmaps were generated as outlined in Chandra et al.[18]. HiC sequencing data was processed with HiC-Pro using parameters ''LIGATION_SITE =GAATAATC,GAATACTC,GAATAGTC,GAATATTC,GAATGATC,GACTAATC,GACTACTC,GACTAGTC,GACTATTC,GACTGATC,GAGTAATC,GAGTACTC,GAGTAGTC,GAGTATTC,GAGTGATC,GATCAATC,GATCACTC,GATCAGTC,GATCATTC,GATCGATC,GATTAATC,GATTACTC,GATTAGTC,GATTATTC,GATTGATC'' and GENOME_FRAGMENT file was generated using ''digest_genome.py -r ^GATC G ^AATC G ^ATTC G ^ACTC G ^AGTC''. ValidPairs generated by HiC-Pro were further converted to cool and hic files. Triangle heatmaps for HiC were generated using Sushi R package (version 1.28.0)

CUT&RUN

CUT&RUN was performed on DP T cells from wild-type, *Gm27162*$^{-/-}$ and CBS +245kbp$^{-/-}$ mice using CUTANA™ ChIC/CUT&RUN Kit (EpiCypher, Cat#14-1048) using manufacturer's recommendation. Briefly, DP T cells were isolated from the thymus via physical dissociation and diluted to yield 0.5 x 10^6 cells per replicate. Nuclei were extracted, washed and allowed to adsorb to activated ConA beads. 0.5 μg of antibody was added, mixed gently and allowed to incubate overnight at 4°C on a nutator. Antibodies used included anti-H3K27ac (Acetyl-Histone H3 (Lys27) (D5E4) XP® Rabbit mAb, CST, Cat# 8173S), anti-H3K27me3 (SNAP-Certified™ for CUT&RUN and CUT&Tag, Rabbit mAb, Cat# 13-0055) and anti-CTCF (Millipore, Cat# 07-729). Following the overnight incubation, reactions were washed with cell permeabilization buffer and incubated with pAG-MNase followed by the isolation of antibody-bound DNA. Two technical replicates were generated for each genotype. Library preparation was performed using NEBNext Ultra II DNA Library Prep Kit for Illumina (NEB) and paired-end sequenced (61bp+61bp) on a NextSeq 1000 (Illumina).

CUT&RUN analysis

FASTQ files from CUT&RUN experiments were analyzed as outlined in Chandra et al.[18]. FASTQ files were first aligned to the bam file using BWA (version 0.7.17-r1188). Mitochondrial chromosome and ChrY were removed during this process using samtools (version 1.11). Duplicated reads were removed using Picard (version 2.26.7) and the bam files were indexed using samtools. BigWig files were generated using bamCoverage (version 3.3.2) with parameters '-normalizedUsing=CPM, binsize=30, smoothLength=300, p=5, extendReads=200'. For peak calling, macs2 (version 2.1.4) was used with following commands: 'macs2 callpeak -t input_file -c control -g mm -n output_path –nomodel -f BAMPE -B –keep-dup all –broad –broad-cutoff 0.25 -q 0.25'. For the background (control), the bam file of IgG CUT&RUN data was used. CUT&RUN tracks were visualized with IGV[46]

Single molecule RNA FISH

Fluorescently labelled oligonucleotide probes complementary to the transcripts of *Ets1* and *Fli1* were designed using the Biosearch Stellaris Probe Designer tool (https://www.biosearchtech.com/support/tools/design-software/stellaris-probe-designer). Probes were designed with 'Masking level' of 5 for high specificity with an 'Oligo length' of 20 nt with 'Min. spacing length (nt)' of 2 nt between probes. Probes targeting *Ets1* transcripts were conjugated with CAL Fluor Red 610 dye (Biosearch Technologies, Cat# SMF-1082-5) and probes targeting *Fli1* transcripts were labelled with Quasar 570 dye (Biosearch Technologies, Cat# SMF-1063-5). Fluorescent probes targeting *Gapdh* transcripts were purchased for use as positive control (Biosearch Technologies, Cat# SMF-3140-1). Both probe sets (5 nmol) were reconstituted in 400 μL 1x TE buffer (10 mM Tris-HCl pH 8.0, 1 mM EDTA) to yield a working concentration of 12.5 uM. Single molecule RNA FISH was performed as previously reported[55] with a few modifications. 3.5 x 10^6 double positive T cells were isolated and deposited on clean poly-L-lysine coated slides for 1 hour at 4°C. Cells were briefly rinsed in cold 1xPBS, fixed in 4% formaldehyde (Fisher Scientific, cat#PI28908) diluted in DEPC treated water for 10 min and then washed twice with 1xPBS. Fixed cells were permeabilized in 0.5% Triton in 1xPBS and Ribonucleoside Vanadyl Complex (NEB, Cat# S1402S) for 15 min and dehydrated in a series of ethanol dilutions ranging from 70% ethanol to 100% ethanol. Slides were rinsed in wash buffer (DEPC treated water, 100% formamide and 20xSSC) for 2 min. Probe hybridization mix (90 uL Hybridization mix, 1 μL/RNA probe and 2 μL RNasin (Promega, Cat# N2615)) was prepared and added to slides, enclosed with a coverslip and sealed with rubber cement followed by overnight incubation at 37°C. The following day, slides were incubated in wash buffer and stained with DAPI before

proceeding to imaging immediately. Cells were imaged across 35 Z planes on average using an inverted Nikon TI-E microscope at 60X magnification.

Single molecule RNA FISH image analysis

RNA FISH images were analyzed using NimbusImage[47] (https://github.com/Kitware/UPennContrast). Nikon multi-stack.nd2 images were uploaded to NimbusImage and automatically segmented using Cellpose with a 'diameter' of 80 pixels. Single molecule RNA FISH spots were automatically identified across all Z planes using built-in deep learning algorithm called Piscis with model 'ps_20240419_112256'. RNA FISH spots were annotated to each cell using the 'Point Count 3D projection' tool and exported as.csv files. Spot counts of *Fli1*, *Ets1* and *Gapdh* mRNA from each cell and imaged location were concatenated using a custom R script which was also used to pool transcript counts into violin plots with statistical significance measured using *wilcox.test()* function in R to compute the p-value for a two-tailed test. Cells with *Gapdh* mRNA count >100 were excluded after visual confirmation of excess noise. Spot counts and the ggplot package in R were used to generate density histograms of *Fli1* and *Ets1* transcript levels (i.e., *geom_density()*) and scatterplots of transcript levels within the same cells were computed using *geom_hex()*.

ORCA experiments

We adapted the method outlined in Mateo et al.,[19] as details are provided below.

Probe design

The *Ets1-Fli1* chromosomal locus, mm10 chr9:32,261,378-33,175,878 were tiled with 30 (30 kbp) barcodes with an average probe density of ~150 primary probes with homology to the chromosomal loci. Each probe is 160 bp long with 20 bp complementary to the fiducial probes, 20 bp barcode sequence, an 80 bp homology to the locus, another 20 bp barcode sequence and finally a 20 bp primer used for probe synthesis. While probes were synthesized for the entire *Ets1-Fli1* locus, we report results between barcodes 3-32 only, which we re-number from 1-30 as the other barcodes were not crucial for the conclusions discussed in this work. The probe library was ordered as an oligo pool from Twist Biosciences.

ORCA hybridization

We followed a procedure adapted from Mateo et al.[19] (see steps 147-166). Cells were washed in 1xPBS for 5 min and permeabilized in 0.5% Triton in 1xPBS for 15 min. This was followed by a dehydration series in 70%, 90% and 100% ethanol for a duration of 2 min each. The coverslips were allowed to dry for 5 min and treated with 4XSSCT/50% formamide (0.6M NaCl, 0.06M sodium citrate, 0.1% Tween-20) at room temperature for 5 minutes, 2.5 min at 95°C in 4XSSCT/50% formamide, and 20 min at 60°C in 4XSSCT/50% formamide. To initiate primary probe hybridization, coverslips were cooled down to room temperature and inverted onto a 60mm dish with hybridization buffer (25% dextran sulfate, 50% formamide, 4% PVSA, 5.6 mM dNTPs, and 10 μg RNaseA) containing 50 μM of ORCA primary probe. Cells were denatured for 2.5 min at 95°C on top of a heating block before being allowed to hybridize for ~16 hrs at 37°C in a humidified chamber. After hybridization, 2XSSCT was added to the 60 mm dish and the coverslip was inverted using forceps, with cells now facing up. Cells were washed in 2XSSCT at 60°C for 15 min followed by a 10 min wash in 2XSSCT at room temperature shaking at 75 rpm. Another 10 min wash was performed at room temperature in 0.2XSSC with shaking at 75 rpm again. The cells were moved to a 2XSSC dish at room temperature while the secondary hybridization buffer (25% dextran sulfate, 10% formamide, and 4% PVSA) with 10 μM fiducial secondary probe was being constituted. The coverslip was inverted into a new 60 mm dish with the secondary hybridization buffer and incubated in the dark for 2 hrs at room temperature. 2XSSCT was added to the dish and the coverslip was re-inverted, cells facing up. The cells were washed in 2XSSCT at 60°C for 5 min and transferred to room temperature 2XSSCT for 10 min shaking at 75 rpm. The cells were washed again in 0.2XSSC for 5 min, rinsed briefly in 2XSSC and stored in a new dish with 2XSSC at 4°C. The dish was wrapped in parafilm and aluminum foil to protect the cells from evaporation and light respectively.

Imaging system setup

All experiments were performed on a Vutara VXL super-resolution widefield microscope (Bruker), which has a 200 μm x 200 μm FOV. Microscope parameters were deposited in the Micro-Meta App.[51] The VXL is composed of a 60X silicon oil immersion objective with a 1.3 numerical aperture (NA), Hamamatsu ORCA-Flash4.0 V3 Digital CMOS camera, infrared-laser based autofocus system, motorized stage and a maximum z-stack size of 20 μm with a z-step size of 150 nm. The fiducial channel was illuminated by a 555-nm solid-state laser and the readout channel was illuminated by a 638-nm solid state laser. Illumination of each of the two channels was supported by a filter wheel consisting of Orange-BP600/50 and Red-BP698/70. Automated sequential labeling was achieved using the PlexFlo multiplexing platform (Bruker). This system contains 15 buffer reservoirs of 2 mL capacity in addition to one 50 mL, two 15 mL, and one 100 mL reservoir. The PlexFlo platform utilizes positive pressure generated from an air pump to drive liquid through 0.02-inch tubing fitted to reduce dead volume. Two 8-way valve systems connect all the reservoirs to the outlet. An imaging chamber (FCS2, Bioptechs) is connected to the PlexFlo fluidic unit to house the 40 mm coverslip with cells and sequentially run labeling steps.

Imaging process

We used the Vutara SRX software (v. 7.3.22) to coordinate the VXL microscope and the PlexFlo fluidics system. First, 2XSSC buffer was flowed into the sample chamber to purge any air bubbles in the system, followed by imaging buffer (0.5 mg/ml glucose oxidase, 40 μg/ml catalase and 10% (wt/vol) glucose in 2×SSC) to select fields-of-view (FOVs) with adequate cell density and low background noise on the readout sample. The first FOV was used to calibrate the infrared autofocus system and the autofocus plane was defined for all subsequent FOVs. Contrary to Mateo et al.[19], we separated readout barcodes from toehold washes to monitor readout signal displacement post-toehold wash. For each readout barcode, we first flowed 1000 μL of 2XSSC solution followed by 800 μL of probe mix which was incubated for 30 min to hybridize. We then treated the cells with two rounds of 1000 μL wash buffer (30% formamide and 2XSSC in water) for 3 min before filling the chamber with 800 μL of imaging buffer. Toehold washes followed readout barcode

sequences and were identical to the fluidics scheme of the readout hybridization. Each FOV was sequentially imaged with the 555-nm and 638-nm lasers in z-stacks of 150 nm steps for a total of 47 steps (~7 μm). This process was repeated 60 times until all the barcodes and toehold steps were imaged. All experiments imaged 20 FOVs where each barcode and toehold step took ~2 hrs. Each FOV was photobleached for 1 min by the 638-nm laser at CTCF boundary nodes to clear accumulating barcode signal and increase the contrast of TAD borders.

Sequential RNA FISH and ORCA

RNA FISH and ORCA experiments were performed as described above, with minor modifications to facilitate both assays within the same cells. First, DP T cells and $CD4^+$ Th1 cells were isolated and deposited on a clean poly-L-Lysine coated coverslip at a concentration of 3.5×10^6 and 1.5×10^6 cells/mL respectively. Cells were allowed to seed for 1 hour at 4°C. Following a brief rinse in 1xPBS, cells were fixed in 4% formaldehyde (Fisher Scientific, cat#PI28908) diluted in DEPC treated water for 10 min and washed twice with 1xPBS. RNA probe hybridization steps and DAPI staining was performed as described above. Following RNA labeling, cells were imaged using the Vutara VXL super-resolution widefield microscope (Bruker), which has a 200 μm x 200 μm field of view (FOV). The coverslip with the RNA labeled sample was loaded into an imaging chamber (FCS2, Bioptechs). During the sample loading process, the back of the coverslip was labeled with a permanent marker on top of patterned dots on the imaging chamber to help with re-alignment during ORCA imaging. For each FOV imaged, the 'x' and 'y' stage coordinates were recorded as a json file prior to the completion of RNA imaging. When RNA FISH imaging was completed, the coverslip was carefully removed from the silicone gaskets and placed in a 60 mm dish with 2xSSC. Prior to ORCA primary probe labeling, cells were treated with RNase A (DNase and protease-free, 10mg/mL, Fisher Scientific, cat#EN0531) solution (50μL RNase A, 50 mL 1xPBS) for 1 hour at 37°C to degrade RNA. Coverslip was briefly rinsed twice in 1xPBS and fixed again in 4% formaldehyde for 10 min at room temperature. Following two rinses with 1xPBS, cells were permeabilized again in 0.5% triton in 1xPBS for 15 min before proceeding to the ORCA primary labeling protocol described above. Following ORCA probe, fiducial and readout labeling, the coverslip was loaded into the imaging chamber with caution taken to re-align the coverslip based on the patterned dots on the back of the coverslip and imaging chamber. The imaging chamber was filled with imaging buffer (0.5 mg/mL glucose oxidase, 40μg/mL catalase and 10% (wt/vol) glucose in 2xSSC) and loaded into the Vutara VXL super-resolution widefield microscope.

RNA FISH FOV re-alignment for ORCA

DAPI image for the first FOV imaged during RNA FISH was used to manually locate the same set of DAPI labeled cells stained during the ORCA labeling protocol. Once the first FOV was manually located, the new 'x' and 'y' stage coordinates from the re-aligned FOV were subtracted from the original RNA FISH FOV stage coordinates to calculate an offset 'x' and 'y' values which accounts for minor re-alignment error during the process of loading the circular coverslip into the imaging chamber. The offset 'x' and 'y' coordinates were applied to all subsequent FOVs to complete the re-alignment process and obtain the same set of cells imaged during RNA FISH. All re-aligned FOVs were manually inspected with the original DAPI stained images from RNA FISH to confirm accuracy of re-alignment. ORCA sequential imaging was started as described above.

QUANTIFICATION AND STATISTICAL ANALYSIS

Statistical analysis

All statistical analyses and data visualization were performed in R (v4.1.1) using custom scripts with the dplyr, ggplot2, UpSetR, and ggsignif packages. For every quantification, the statistical test used, the exact value of *n*, and what *n* represents are reported in the corresponding figure legend, and additional detail on each computation is provided under method details. Comparisons of mRNA counts and of 3D distance distributions between genotypes or interaction groups were assessed with the two-sided Wilcoxon rank-sum (Mann–Whitney *U*) test, implemented with the wilcox.test() function in R (alternative = "two.sided") and annotated with geom_signif(). Because mRNA count and inter-centroid-distance distributions are non-normal, non-parametric tests were used throughout and no assumption of normality was made; distributions are summarized by their median (and, where noted, mean) and shown in full as violin/box plots, cumulative distribution functions, or ridge plots. Differences were considered significant at $P < 0.05$. Correlations between HiC and ORCA contact-frequency matrices, and between *Ets1* and *Fli1* mRNA levels, were quantified by Pearson's *r* (and Spearman's *r* for the HiC–ORCA median-distance comparison), as reported in the figure legends. Only full traces with all 30 readouts detected were used for contact-threshold, multi-way-interaction, radius-of-gyration, and entropy analyses. To control for differing trace numbers between genotypes, bootstrapped comparisons of local compaction ($\log_2$ fold change in radius of gyration) and of per-readout entropy were computed by randomly sampling 1,000 traces per genotype (for entropy, sampling with replacement over 100 iterations); entropy differences are reported with their 95% confidence interval.

Preprocessing and spot registration

Images acquired on the Vutara SRX software (v. 7.3.22) were converted to TIFF files for each FOV in the 'xyzct' format, where 'xy' are the dimensions of each image, 'z' is the stack recorded, 'c' is the field-of-view (FOV) index and 't' is the time point at which the image was taken. For each FOV TIFF file, we performed pre-processing to remove areas of high-intensity readout signal that impacts spot calling and registration. We first produced maximum intensity projection images combining z-stacks for each FOV and timepoint, producing two images for the fiducial and readout channels respectively. Next, we performed cell segmentation using the 'cyto' model of Cellpose (v. 2.2.2) running on python (v. 3.8.17) and torch (v. 2.0.1+cu117) to create a mask of objects passing the mean diameter threshold. The original mask was then dilated using a 'disk' structuring element with a radius of 10 to extend the

masking area around each cell. A final mask was constructed by intersecting the masked areas from the fiducial and readout channel masks for each FOV. The final mask was superimposed on the original TIFF images of each channel and subtracted to produce a series of masked TIFF files with only the cells of interest. The masked TIFFs for each FOV and time point were again processed into maximum intensity projections and converted to DAX files for compatibility with the spot detection software. Since the Vutara VXL microscope settings are not auto-detected in step 205, we adjusted the 'nmPixXY' and 'pix_to_mm' values to '108' and '9.30' respectively to reflect the microscope setup we are using. Drift correction, spot detection and registration was performed using 'ChrTracer3' outlined in steps 202 onward in Mateo et al.[19]

RNA FISH – ORCA cell registration

For realigning the RNA FISH and ORCA spots on a per cell basis, we followed a procedure adapted from Mateo et al.[19] with modifications implemented for the Vutara VXL super-resolution widefield microscope. Briefly, RNA FISH and ORCA images acquired on the Vutara SRX software (v. 7.3.22) were converted to TIFF files for each FOV in the 'xyzct' format, where 'xy' are the dimensions of each image, 'z' is the stack recorded, 'c' is the field-of-view (FOV) index and 't' is the time point at which the image was taken. In order to assign a common cell ID unifying the RNA FISH and ORCA data to the same cells, we used MATLAB (MathWorks, v.R2022a) to parse the RNA FISH DAPI, *Ets1* mRNA and *Fli1* mRNA channels, convert to z-stacks per channel, made maximum projected images and used Cellpose (v. 2.2.2) on the DAPI images to create a mask capturing the cell boundaries. The ORCA images for DAPI, fiducial and readout channels were converted to zstacks, max projected per channel and timepoint. Cellpose was used on the DAPI max projected images per timepoint and FOV imaged to create a mask capturing the cell boundaries. The RNA FISH and ORCA Cellpose masks were aligned per FOV using 'CorrAlignFast_DAPI' MATLAB function from Mateo et al.[19]. This MATLAB script generates a matrix capturing the 'xshift', 'yshift' and rotation (i.e., 'theta') offsets which was applied to align the ORCA DAPI mask to the RNA FISH DAPI mask. In addition, aligned RNA FISH – ORCA DAPI image composites were generated for each FOV to visually confirm the accuracy of re-alignment per cell.

Prior to running the final MATLAB script, the RNA FISH images were analyzed on NimbusImage (https://github.com/Kitware/UPennContrast) as described in the single molecule RNA FISH image analysis with a few modifications. Instead of recording the *Ets1* mRNA and *Fli1* mRNA count per cell, NimbusImage (i.e., 'point count' algorithm within 'Measure Objects') was used to record the 'x' and 'y' coordinate of each *Ets1* and *Fli1* mRNA spot detected using the Piscis spot counting tool. All spot coordinates across all FOVs were exported as a CSV file. In parallel, we analyzed the ORCA imaging data using ChrTracer3 for drift correction, ORCA spot detection and registration as outlined in step 202 onwards in Mateo et al.[19].

We next used MATLAB to read the RNA FISH Cellpose mask, ORCA Cellpose mask, alignment offset matrix, RNA FISH spot coordinates (for *Ets1* and *Fli1* mRNA separately) and ChrTracer3 spot coordinates for fiducial and readout channels. The alignment matrix was used to apply an offset to the RNA FISH and ChrTracer3 ORCA spot coordinates. The aligned RNA FISH and ORCA DAPI masks were assigned cell IDs and matched to the offset RNA FISH and ChrTracer3 spots based on intersecting 'x' and 'y' coordinates within the cell mask area. Cells on the boundaries of each FOV were excluded if the final offset coordinates exceeded the total height and width of the FOV. We generated 3 CSV files with a unique cell ID assigned to each coordinate of the *Ets1* and *Fli1* mRNA data, along with cell ID annotated to each ORCA chromatin trace. We used R to compute the 3D distance between the readout coordinates corresponding to *Fli1-Ets1* promoter, *Ets1-Gm27162* and *Fli1-Gm27162*. We used R to sum all *Ets1* and *Fli1* mRNA given a specific cell ID and then merged the mRNA counts to the 3D distance matrix based on the common cell ID.

Contact threshold determination

In order to avoid using an arbitrary distance threshold to define contact, we computed the average distance between the centroids of adjacent steps/readouts as the threshold for calling two chromatin regions in contact.[21] We filtered chromatin traces that had all successful hybridizations imaged (i.e., 30 out of 30 hybridizations imaged and registered to the same chromatin trace). This data-driven approach was used to compute the contact threshold for all the cell types and genotypes in this study. The thresholds computed were applied for all analyses within our study requiring the explicit definition of a contact threshold – wild-type DP T cells ($D_{threshold}$ = 257.89 nm), *Gm27162*$^{-/-}$ DP T cells ($D_{threshold}$ = 260.99 nm), CBS +245kbp$^{-/-}$ DP T cells ($D_{threshold}$ = 262.13 nm), wild-type CD4^{+} Th1 cells ($D_{threshold}$ = 280.98 nm) and *Gm27162*$^{-/-}$ CD4^{+} Th1 cells ($D_{threshold}$ = 297.60 nm).

Contact between *Fli1*, *Ets1* and *Gm27162*

For the 3-way contact analyses in Figures 2F, 3F, 4F, and 6F, we computed the centroids of the ORCA nodes corresponding to *Fli1* (nodes 7-9), *Ets1* (nodes 15-17) and *Gm27162* (node 22) in each chromatin trace across wild-type, *Gm27162*$^{-/-}$ and CBS +245kbp$^{-/-}$ DP T cells and CD4^{+} Th1 cells using a custom R script. We used *dplyr()* to merge the centroid tables from each genotype and calculated the 3D Euclidean distances between each pair of centroids (*Fli1* to *Ets1*, *Fli1* to *Gm27162* and *Ets1* to *Gm27162*). To determine contact, we used distance thresholds derived from ORCA data for each genotype (described above) and classified the chromatin traces into different interaction categories based on the number of pairwise distances below the threshold. For instance, if all centroid distances for a given chromatin trace were below contact threshold, the traces were classified as having 'three-way' interactions. For visualization, we used the *UpSetR()* package in R to display the interaction network between the three centroids across the genotypes. In addition, we generated cumulative distribution function (CDFs) and ridge plots using *ggplot()* in R to display the contact threshold-independent distribution of the three centroid distances in Figures 2D, 3D, and 4D for wild-type, *Gm27162*$^{-/-}$ and CBS +245kbp$^{-/-}$ DP T cells respectively. For Figure 6F, we used *ggplot()* to show the interaction combinations as a stacked barplot.

Acetylated-methylated domain contacts

We computed the interaction between acetylated and methylated domain pairs by first selecting ORCA nodes corresponding to methylated domain #1 (nodes 3-4), acetylated domain (nodes 15-17) and methylated domain #2 (nodes 29-30) previously annotated in Figure 1A. As before, we computed the centroids of the ORCA nodes per chromatin trace across wild-type, *Gm27162*$^{-/-}$ and CBS +245kbp$^{-/-}$ DP T cells using R. We used *dplyr()* in R to merge the centroid tables from each genotype and calculated the 3D Euclidean distance between the pairs of centroids (i.e., methylated domain #1 to acetylated domain, methylated domain #1 to methylated domain #2 and acetylated domain to methylated domain #2). We generated cumulative distribution function (CDF) and ridge plots using *ggplot()* to display the distribution of centroid distance pairs for wild-type, *Gm27162*$^{-/-}$ and CBS +245kbp$^{-/-}$ DP T cells respectively. In Figures 3E and 4E, we included the wild-type distributions to draw direct comparisons with CBS +245kbp$^{-/-}$ and *Gm27162*$^{-/-}$ distributions respectively.

Radius of Gyration (R_g)

We computed the radius of gyration as previously described[21,23,29] to quantify the compaction of chromatin domains within the *Ets1-Fli1* multi-enhancer hub in Figures 3G, S2F, S3F, and S5D–S5F. The radius of gyration was measured by computing the average squared distance of all ORCA readout coordinates (x,y,z) from its center of mass, where r_i is the position vector of the i^{th} point and r_{CM} is the center of mass position vector:

$$R_g = \sqrt{\frac{1}{N}\sum_{i=1}^{N}(\overrightarrow{r_i} - \overrightarrow{r_{CM}})^2}$$

Acetylated-methylated domain compaction

To compute the changes in compaction between acetylated and methylated domains in Figure S3F, ORCA readouts corresponding to the acetylated domain (nodes 06-17) and methylated domains (nodes 23-30) were first extracted and used to compute the center of mass using all nodes in the respective groups. Next, we calculated the squared distance of each readout from the center of mass, took the mean and computed the square root to obtain the radius of gyration using the equation above in R. We plotted the two-dimensional hexbin heatmap using *geom_hex()* in R to compare the correlation between the compaction of acetylated and methylated domains.

Compaction between *Fli1* and *Ets1*

We used the ORCA nodes corresponding to the *Fli1-Ets1* window (nodes 06-17) to compute the radius of gyration for each chromatin trace within wild-type and CBS +245kbp$^{-/-}$ DP T cells. We randomly sampled 1000 chromatin traces from each genotype and computed the $\log_2$(fold change) in the *Fli1-Ets1* radius of gyration between the two genotypes. We used R to plot the density barplot displaying the $\log_2$(fold change) difference in *Fli1-Ets1* window compaction in Figure 3G.

Compaction between *Ets1* and *Gm27162*

We used the ORCA nodes corresponding to the *Ets1-Gm27162* window (nodes 15-22) to compute the radius of gyration for each chromatin trace within wild-type and *Gm27162*$^{-/-}$ DP T cells and CD4$^+$ Th1 cells in Figures S5D–S5F. We used *ggplot()* in R to plot the cumulative distribution function (CDFs) to display the contact threshold-independent distribution of *Ets1-Gm27162* local radius of gyration.

Entropy

We computed the average entropy per readout as described prior. For each genotype in Figure 6G, we first filtered the dataset to include only full-trace alleles, defined as those containing all 30 readouts detected. We then implemented a bootstrapping approach to select 1000 chromatin traces with replacement for 100 iterations. We next compute the Euclidean distance matrices between all readout positions (x,y,z) for each trace. We normalize the cumulative distance matrix into probability distributions and then compute the entropy per readout pair using the formula:

$$S_{i,j} = -\sum P(x_i)\log_2 P(x_i)$$

For each readout, we computed the mean entropy and calculated the entropy difference between wild-type DP T cells and *Gm27162*$^{-/-}$ DP, wild-type CD4$^+$ Th1 and *Gm27162*$^{-/-}$ CD4$^+$ Th1 cells. We used R to plot a line plot of the entropy difference by our perturbation condition and plot the 95% confidence interval per readout.

Radial position trace clustering

For each genotype in Figure 6J, we randomly sampled 1000 chromatin traces to normalize for the different trace numbers per genotype. For each chromatin trace, we used R to compute the geometric center and then computed the 3D distance of each readout to this center. Using a distance threshold of 200 nm, we binarized the 30 readout distances into a vector with values '1' if the readout distance is within the threshold and '0' if the readout falls out of the threshold distance. We used R to repeat this computation across

all 1000 chromatin traces per genotype, summed the binary vector and computed the allele frequency by dividing the summed readout counts by the total number of alleles analyzed (i.e., 1000). We next used *ggplot()* to generate a barplot and assigned colors to regulatory elements within the locus, particularly readouts 11, 23, 28 (CTCF binding sites, 'green'), readout 10 (*Fli1* promoter, 'red'), readout 15 (*Ets1* promoter, 'yellow') and readout 22 (*Gm27162*, 'blue'). All other readouts were colored 'grey'. We used *geom_text()* to annotate the frequency labels for the regulatory elements described above. In addition, we used *facet_wrap()* to combine the bar charts of all genotypes into the same figure.

Interaction-based allele clustering

Before clustering cells based on the interaction state between *Ets1*, *Fli1* and *Gm27162*, we first used R as mentioned above to compute the ORCA contact threshold for all cell types in the RNA FISH and ORCA experiments. The thresholds computed were applied for all RNA and ORCA analyses within our study requiring the explicit definition of a contact threshold – wild-type DP T cells ($D_{threshold}$ = 298.4 nm), *Gm27162*$^{-/-}$ DP T cells ($D_{threshold}$ = 296.7 nm), wild-type CD4^{+} Th1 cells ($D_{threshold}$ = 339.6 nm) and *Gm27162*$^{-/-}$ CD4^{+} Th1 cells ($D_{threshold}$ = 321.4 nm).

Clustering in Figures 5G, 7C, S4E, and S6D were performed in R using *dplyr()*. First, the distance matrices for either the DP T cell or CD4^{+} Th1 cells were merged by genotype. This distance matrix also included '*Ets1_mRNA_count*' and *'Fli1_mRNA_count'* data. Next, we categorized each allele per genotype into groups depending on the number of pairwise distances below the threshold. For instance, an allele was assigned to the 'No interaction' category if the *Ets1-Gm27162*, *Fli1-Gm27162* and *Ets1-Fli1* distances (in nm) was greater than the threshold for that particular genotype. At this stage, cells were grouped by interaction category, genotype and its mean and median expressions were computed using the *mean()* and *median()* functions native to R. We used *geom_jitter()*, *geom_violin()* and *geom_boxplot()* to visualize the distribution of *Ets1* and *Fli1* mRNA per interaction group. The number of cells within each category was annotated on the violin plot using *geom_text()*. Significance was computed using *geom_signif()* using the 'wilcox_test' with the alternative set to 'two.sided'.

The pie chart in Figures 5H and 7D were computed using a similar methodology mentioned above, with one modification after clustering based on interactions. Cells with high *Ets1* levels (>25 mRNA molecules) were filtered using *dplyr()* across all interaction categories. Pie chart was created using *ggplot()* in R.

Ets1/Fli1 mRNA $\log_2$ (fold change)

For each genotype, we used R to first add 1 to the *'Ets1_mRNA_count'* and *'Fli1_mRNA_count'* per genotype to avoid division by zero when computing the $\log_2$ fold change. Each cell was grouped by 'fov', 's', 'cellID' and the ratio of *Ets1* mRNA over *Fli1* expression was computed. Within the same grouping, we used *dplyr()* to compute the $\log_2$ (fold change) of the ratio of *Ets1* and *Fli1* mRNA expression per cell. We used *ggplot()* to generate a ridge plot showcasing the distribution of the $\log_2$ (fold change) across each cell type and genotype in Figure 7B. We used *geom_density()* and *geom_vline()* to normalize for cell number differences across all the categories and display the mean value of the $\log_2$ (fold change) respectively.